

K. Baird, F.-J. Decker, M. J. Hogan^{*}, R.H. Iverson, P. Raimondi, R.H. Siemann, D. Walz

Stanford Linear Accelerator Center

B.E. Blue, C.E. Clayton, E.S. Dodd, C. Joshi^{*}, K.A. Marsh, W.B. Mori, S. Wang

University of California at Los Angeles

T. Katsouleas^{*}, S. Lee, P. Muggli

University of Southern California

R. Assmann

CERN

E-162: Positron and Electron Dynamics in a Plasma Wakefield Accelerator

I Introduction

Extraordinarily high fields are generated in beam-plasma interactions. Accelerating gradients in excess of 100 GeV/m and focusing gradients greater than 1 MT/m have been observed. These results show the promise of plasma devices for high-energy accelerators, but much of this promise has yet to be realized in components or systems that could be part of an operating accelerator. This is a proposal to study key questions related to the applicability of plasmas to high-energy accelerators.

High gradient accelerators are almost always thought of in the context of linear colliders. SLAC experiment E-157, performed by this group, was the first experiment to study plasma wakefield acceleration (PWFA) of electrons over meter-scale distances. This length is probably close to that of an accelerator stage, and E-157 was the study of issues that arise in a first, primitive prototype of a plasma accelerator stage. Positron-plasma interaction physics is qualitatively different, and we are proposing to make the first measurements of positrons in meter-scale plasmas. We have learned a great deal about beam-plasma experiments during the course of E-157, and the proposal includes a substantial improvement to the E-157 apparatus. Therefore, we are also proposing to use this apparatus to improve our earlier electron measurements.

^{*} Primary Investigator

E-157 was the first experiment to study plasma wakefield acceleration of electrons over meter-scale distances. The experiment was proposed in 1997 with the primary goal of measuring acceleration by an electron beam-driven plasma wave. E-157 data taking was completed in the Spring of 2000 and has observed a rich variety of effects (summarized in Table 2 and Section VII). The collaboration has developed a unique facility at the SLAC Final Focus Test Beam, and we have experience and expertise in these experiments. All of this experimental work is performed in conjunction with the theory and simulation that are essential for understanding.

The interaction of intense positron beams in long plasmas has never been systematically studied experimentally, and there is an opportunity at SLAC for groundbreaking experiments. We expect that the collective phenomena taking place in plasmas subject to intense positron beams—and the resultant reaction back onto the beam itself—to be radically different than for electron beams. This is due to the difference in the sign of the forces between the mobile plasma electrons and beam particles. For example, for beam densities higher than the plasma density, an electron beam will expel all the plasma electrons in a time-scale given by the inverse of the beam plasma frequency (ω_{pb}). This leaves a pure ion column that becomes a rather simple optical element for the electrons. However, for similarly intense positron beams, the background plasma electrons must rush in to neutralize the positron beam leaving a rather complex field structure for the positrons trailing by more than c/ω_{pb} behind the head of the beam.

Understanding these differences is essential for application of plasmas to high-energy accelerators. A positron beam of the same intensity as the electron beam in E-157 is available to the same experimental apparatus. This presents a unique and timely opportunity for looking at, plasma focusing and wakefield acceleration of positron beams, and perhaps undiscovered basic physics, such as the refraction of an electron beam at a plasma–gas interface [Appendix 3].

The E-157 plasma source and beam diagnostics (see Figure 1), presently situated at IP1 (Interaction Point 1) of the Final Focus Test Beam (FFTB), offer a chance for an immediate first look at many of the physics issues associated with propagation and acceleration of positrons in a long plasma. A more detailed characterization of the accelerating wakes of both electrons and positrons will then be possible by moving the

experiment upstream to IPO (Interaction Point 0). The magnetic optics upstream of IPO will enable, for the first time, the study and propagation of a matched beam in a long plasma. The remaining optics downstream of the plasma will combine with the FFTB dipole dump magnets to form an imaging spectrometer. An imaging spectrometer will decouple the effects of the transverse and longitudinal wakes, which have complicated the interpretation of previous data.

II Linear Theory

We begin by summarizing the results of linear wakefield theory ($n_b/n_0 \ll 1$) to introduce many of the important physical mechanisms for PWFA. Linear wakefield theory has been validated by detailed computer simulations and several experiments and applies equally to electrons and positrons. 2-D and 3-D Particle in Cell (PIC) simulations will be used to better describe the non-linear regime in which the experiments are performed.

Table 1: Legend of symbols used in this proposal

Physical Parameter	Symbol
Speed of Light in Vacuum	c
Charge of an Electron	e
Accelerating Gradient	eE
Plasma Focusing Gradient	$K = \omega_p / (2\gamma)^{1/2} c$
Plasma Wavenumber	$k_p = \omega_p / c$
Plasma Wavelength	$\lambda_p = 2\pi / k_p$
Mass of an Electron	m_e
Number of Electrons per Bunch	N
Drive Beam Density	$n_b = N / (2\pi)^{3/2} \sigma_r^2 \sigma_z$
Plasma Density	n_0
Hollow Channel Radius	r_0
Drive Beam Transverse Size	σ_r
Drive Beam Bunch Length	σ_z
Beam Plasma Frequency	$\omega_{pb} = (n_b e^2 / \epsilon_0 m_e)$
Electron Plasma Frequency	$\omega_p = (n_0 e^2 / \epsilon_0 m_e)$

In linear theory, the response of a plasma to a relativistic bunch with bi-Gaussian density distribution is given by integrating the Green's function for a single electron. The result can be expressed approximately by

$$eE[eV/cm] = \sqrt{n_o[cm^{-3}]} \times \frac{n_b}{n_o} \frac{k_p \sigma_z e^{-k_p^2 \sigma_z^2} \sqrt{2\pi}}{1 + \frac{1}{k_p^2 \sigma_r^2}} \quad (1)$$

Equation (1) predicts the maximum wake amplitude to occur for a plasma density such that $\lambda_p = 4\sigma_z$ for $k_p \sigma_r \ll 1$. For this optimum plasma the wakefield amplitude can be expressed as

$$eE[MeV/m] = 240 \times \frac{N}{4 \times 10^{10}} \times \frac{0.6}{\sigma_z[mm]}^2 \quad (2)$$

From this we see that the maximum wake amplitude for a given amount of charge scales as $1/\sigma_z^2$.

For typical parameters of the SLC bunch and the plasmas of interest for high gradient acceleration, the limits of the linear theory are exceeded. In fact, n_b/n_o is greater than one and $eE/m\omega_p c$ is on the order of one for this example. Thus, we turn instead to fully nonlinear particle-in-cell (PIC) numerical simulations.

III PIC Simulations

There is no experimental data on wakes generated by intense positron beams in a plasma. The physical mechanism behind generating such wakes with positrons is different than with electrons. In the regime of linear wakefield theory, the wavelengths and amplitudes of wakes from positron and electron beams are identical, but when the beam density is larger than the plasma density, linear theory breaks down and there is an asymmetry between the electron and positron cases. In the electron case the beam electrons blow out the plasma electrons whereas in the positron case the beam positrons suck in the plasma electrons.

The previous simulations for electron beam drivers (see Appendix 1) have been extended by considering positrons. To make connection to the previous work and illustrate the different dynamics associated with positron drivers, the wake structure of a positron bunch is compared with the wake of an electron bunch. The phenomena

illustrated in the following Figures highlight much of the interesting physics and serve as a guide to what we will measure in the experimental program outlined in Section VI.

Transverse Dynamics

Figure 2a shows the electron beam envelope undergoing three envelope oscillations within the plasma due to the transverse focusing fields of the ion column (“blow out” regime), which corresponds to a focusing gradient on the order of 4,000 T/m. We can not measure these oscillations within the plasma; instead we make the equivalent measurement of spot size at the downstream OTR as a function of plasma density. Figure 2c shows the electron beam transverse size measured at the downstream OTR as a function of the betatron phase advance of the beam in the plasma ($(n_0)^{1/2}$). The green curve shows the expected envelope oscillations based on the given beam parameters. The good agreement demonstrates that for the bulk of the electron beam, the transverse focusing fields in the plasma can be represented as a strong but simple thick lens. Figure 2b shows the expected beam envelope behavior for a positron beam within the plasma. The constant focusing force of the ion column in the electron case is replaced by a dynamic focusing structure resulting from regions of different plasma electron density. Characterizing the dynamic focusing force resulting from electrons being sucked in by the positron drive bunch is one of the first goals of this proposed experiment and would fill in the missing panel Figure 2d.

Longitudinal Dynamics

Figure 3 (a) and (b) show the longitudinal wake structures for electron and positron bunches in a 3-D simulation. Physical beam parameters similar to those available in the FFTB are used to illustrate the expected physical behavior. Simulations tailored to the exact parameters of the experiment will be performed as these parameters are determined in the operation of the experiment. For $N = 2 \times 10^{10}$, $\sigma_z = 0.4 \text{ mm} (\sim 1.3 \text{ ps})$, the plasma density $4.34 \times 10^{14} \text{ cm}^{-3}$ is chosen to optimize the accelerating field ($E_p \sim 4 \text{ MV/m}$). The positron beam density is larger than the plasma density (i.e., the plasma is referred to as being in the “underdense regime”). In this regime, the plasma electrons are sucked in by the space charge of the positron driver, and their momentum takes them back out. In contrast to the electron beam case, the positron wake is less steep in the back of the bunch. In the electron case, the plasma electrons blown out by the head all rush back in to

the tail of the bunch at the same time producing a large spike in accelerating gradient. For the positrons however, plasma electrons are continually being sucked in and a smaller spike is generated.

In the 3-D simulations shown in Figure 3 (electrons in Figure 3a, positrons in Figure 3b) the beam has been propagated into the plasma roughly 1.6cm to let the longitudinal wakes develop, and gives the accelerating gradients and an energy spectrum when extrapolated to 1.4m. Positrons in the tail of the beam in the maximum energy bin have a bin-averaged gradient of 192 MeV/m. The electron-driven case with the same parameters shows a maximum bin-averaged gradient of 340 MeV/m. When scaled to a bunch length of 0.65mm, the gradients are correspondingly lower: 75 MeV/m for positrons and 130 MeV/m for electrons. Further, the ratio of accelerating fields to de-accelerating fields known as the transformer ratio is 1.2 for the positron case, considerably lower than for the electron beam driver. To experimentally characterize these accelerating wakes in detail, a high-resolution energy spectrometer is required. The creation of the imaging spectrometer is the primary motivation for moving the experiment upstream to IP0 in the FFTB (discussed in Section IV).

Hollow Plasmas

The primary limit to positron wake amplitude, as seen in Figure 3b is the smearing of the plasma density peak on the axis due to plasma electrons from different radii arriving at different times. These effects can be mitigated by using a plasma in the shape of a hollow cylinder or channel. A hollow channel plasma can be made by UV ionization of a long gas column with a laser beam for which the center is blocked. To investigate the feasibility of creating such a hollow plasma, the reflective coating of a UV mirror was purposely damaged over a $\sim 500\ \mu\text{m}$ diameter and the E-157 UV laser beam was reflected off the mirror. Figure 4 shows an images of the UV laser profile $\sim 30\ \text{cm}$ (Figure 4a) and $\sim 1\text{m}$ (Figure 4b) from the mirror. Diffraction of the UV beam has not yet filled in the hole and it thus seems possible to create the desired hollow profile over the length of the plasma.

Positron and electron wakes in a hollow plasma channel of various radii have been studied through simulation. The results of the wake amplitude vs. radius of the channel are shown in Figure 5. Note that the amplitude of the positron wake increases as

the channel radius increases. Interestingly, the non-linear wake profiles for positrons and electrons reverse roles in the hollow and homogeneous plasmas. The wake of the positron driver becomes spiked on the axis in the hollow plasma channel, resembling the nonlinear spike of electron wakes in a homogeneous plasma. On the other hand, the electron wake in a hollow plasma channel loses the narrow spike seen in Figure 3a for a homogeneous plasma.

Summary

We have studied positron wakes with PIC simulations and illustrated many of the experimental signatures we seek to measure. The transverse wakes for a positron bunch are dynamic throughout the length of the bunch, resulting in qualitatively different transverse dynamics. The accelerating wake of a positron bunch is smaller than that of an electron bunch in an homogenous plasma, but it can be made comparable to the electron wake by employing a hollow plasma.

Experience has shown that the simulations give good guidance, but in practice the phenomena are more complex. Experimentation is critical to understand the value of plasmas to high-energy colliders.

IV Beam Properties

As mentioned in the introduction, E-157 was the first experiment to study the issues associated with PWFA in a long plasma. The experimental techniques and apparatus of E-157 were developed and improved over the course of five runs distributed from the Summer of 1998 to the Spring of 2000. In contrast to E-157, which was started from no experience in electron plasma interactions, the experiments proposed here will benefit from and continue to build upon the extensive experience and infrastructure developed over the past two years. Results from E-157 are discussed in section VII.

E-157 was able to operate under a wide variety of experimental conditions (beam and plasma densities) at a beam repetition rate of 1Hz. The beam rate of 1 Hz was dictated by the data acquisition system and mitigating damage to the pellicle mirrors (discussed in the Section V). With the experimental apparatus situated in it's current location (IP1), typical beam parameters are $E=28.5$ GeV, $z=0.7$ mm, $N=2 \times 10^{10}$ electrons/bunch and $r=40-100$ μ m. These parameters are useful for studying the majority

of the physics associated with beam-driven PWFA. Positron beams with the same energy, bunch length, and charge have already been delivered to the FFTB for the E-150 SLAC experiment. Sending this positron beam down the FFTB into the existing E-157 apparatus would allow a first look at the transverse dynamics of a positron beam propagating in a long plasma. With the current E-157 diagnostics all working and at a mature stage of development, a reasonably complete study of the transverse dynamics of an unmatched positron beam could be concluded in a relatively short time.

Subsequently moving the experimental apparatus upstream to IP0 offers two important advantages. Firstly, the magnetic optics available upstream from IP0 would provide the ability to match the beam into the plasma and contrast the behavior with the unmatched case. Secondly, the remaining quadrupoles located downstream from the plasma exit can be used in conjunction with the FFTB dipole dump magnets to form an imaging spectrometer. An imaging spectrometer will de-couple the effects of transverse and longitudinal wakes, allowing for a more detailed examination of the energy spectrum produced by the plasma. Our E-157 experience has shown this to be a significant experimental issue.

Moving the E-157 equipment upstream to IP0 requires only minor modification to the existing beam line. Two quadrupoles (6020-6030) must be removed to create the necessary space. Solutions exist that use the remaining quadrupoles (6040-6080) to image the beam exiting the plasma onto the Cherenkov radiator(see next section). We estimate that one to two weeks would be required to restore these quadrupoles and associated mounts

V Plasma source and diagnostics

The experiments proposed here rely on the E-157 experimental apparatus, presently located at IP1 in the FFTB, and shown schematically in Figure 1. The details of the apparatus as well as many of the experimental issues are described in Appendix 2. The hardware summarized below is working and can be transported as a package to IP0 for the second and third group of measurements discussed in Section VI.

A 1.4 m long lithium (Li) heat pipe oven produces a Li vapor with a density $\rho_0 \sim 3 \times 10^{15} \text{ cm}^{-3}$. The vapor is contained by a He buffer gas and isolated from the beamline

vacuum via thin Be windows. The plasma is produced by ionizing the vapor with a 193nm Argon-Fluoride (ArF) excimer laser located nearby. The laser beam is injected into and extracted from the plasma by thin pellicles that are also traversed by the electron beam. The fluorescence of the pellicle silica substrate when traversed by the particles, and its fluorescence when hit by the UV laser pulse are viewed on a single screen to align the electron beam and the laser beam (i.e., the plasma) both upstream and downstream of the Li column. Roughly 15% of the Li vapor is ionized and the plasma recombination time is of the order of 15 μ s. Varying the laser discharge voltage and/or delay between the laser pulse and electron beam provide convenient controls of plasma density. The initial plasma density is measured by means of the incident UV energy on a shot-by-shot basis.

Titanium (Ti) foils provide another key feature of the experiment. Optical transition radiation (OTR) from the electron beam passing through the Ti is detected both upstream and downstream of the plasma. OTR allows monitoring of the electron beam profile and gives the information needed for measuring and removing beam tails. Plasma focusing is studied by measuring the beam size after the plasma.

The plasma is followed almost immediately by the FFTB permanent magnet dump which introduces energy dispersion in the vertical plane. An aerogel Cherenkov radiator with index of refraction $n = 1.009$ is located after the dipole dump magnets. The dispersion at the aerogel is $y = 100$ mm. Light from this radiator is transported out of the FFTB tunnel to an optical table where the time integrated spot size and the time dispersed horizontal and vertical profiles are measured. The latter is done with a streak camera. The time dispersed vertical profile gives the energy spectrum of the beam with 1 ps time resolution. This time resolved energy measurement is the key to studying the energy changes within the bunch.

Data is acquired with shot-by-shot correlations. The upstream and downstream OTR images, the time integrated Cherenkov image, the streak camera image, and laser and beam data are acquired on each shot, and information from these different diagnostics can be combined for filtering and sorting of data.

VI Experimental Program

Run 1: A First Look at Positron Propagation in Long Homogeneous and Hollow Plasmas.

IP1 – 4 weeks

Use the functioning E-157 apparatus currently located at IP1 to characterize the transverse wakes of a positron driven plasma wave in the “suck-in regime” of a homogeneous plasma. Envelope oscillations will be studied as a function of plasma density. The time dependent focussing forces within the positron bunch will be resolved via the Cherenkov/streak camera diagnostic at IP2. A hollow channel plasma will be made by introducing a mask in the ionization laser pulse. The transverse dynamics (time integrated and time resolved) will be measured as a function of channel radius and compared to the case of homogeneous plasmas.

Extended break to move to IP0 – 8 weeks

Access to the FFTB tunnel will be required during this time.

Run 2: High Resolution Energy Gain Measurements of Positrons

IP0 – 6 weeks

The quadrupoles downstream of IP0 are used in conjunction with the FFTB dipole dump magnet to form an imaging spectrometer. The detailed structure of the longitudinal wakes will be resolved within the bunch and compared with theory. The incoming beam density required to minimize filamentation and maximize acceleration will be explored for a homogeneous plasma. The accelerating wake produced in a hollow channel plasma will be compared to the homogeneous plasma case and to the numerical simulations.

Run 3: High Resolution Energy Gain Measurements of Electrons

IP0 – 4 weeks

The primary goal of E-157 was to measure 1 GeV acceleration of electrons from an electron beam driven plasma wave. As the experimental parameters evolved (principally the electron bunch charge and bunch length) and our understanding of the physics progressed, the magnitude of the accelerating gradient has gone down. However, the underlying physics is unchanged, and we have learned a tremendous amount about

plasma accelerators from this experiment. Moving the experiment to IP0 will provide two advantages over the original design that build on the experience gained from E-157. First, the magnetic optics upstream of IP0 will allow the study of matched beam propagation of electrons in a long plasma for the first time. Second, the imaging spectrometer will allow for a more detailed measurement of the accelerating wakes than were possible in E-157 without an imaging spectrometer.

VII E-157 Results

E-157 was proposed in 1997, began running in the summer of 1998, and concluded data taking in the spring of 2000. The experiment has yielded an enormous amount of data that is still being analyzed. Table 2 highlights the experimental work in progress and the text that follows gives a brief description of the individual elements.

Table 2: E-157 Publications in Progress

Experimental Result	Publication or Expected Submissions(*)
E-157: A 1.4 Meter-long Plasma Wakefield Acceleration Experiment Using a 30 GeV Electron Beam from the Stanford Linear Accelerator Center Linac	Physics of Plasmas 7, 2241 (2000)
Refraction of an Electron Beam at a Plasma–Gas Interface	Nature (submitted)
Gas/Plasma Cherenkov Radiation as a Diagnostic of Plasma Density	Phys. Rev. Letters*
Transverse Betatron Dynamics of a 30 GeV Beam in a Long Plasma	Phys. Rev. Letters*
Experimental Test for the Electron Hose Instability	Phys. Rev. Letters*
X-ray Generation from an Ion Channel Wiggler	Phys. Rev. Letters*
High-Gradient Acceleration of Electrons in a Meter-Long Plasma Wakefield Accelerator	Science*

Refraction of the Electron Beam at a Plasma–Gas Interface

The observation of refraction of the electron beam as it exits the plasma/gas boundary, defined by the laser path, was among the unanticipated results of E-157. This refraction is analogous to the bending of light exiting a water/air interface; however the associated Snell’s law is time-dependent and non-linear. Three-dimensional plasma

simulations have been crucial for understanding and interpreting all of these measurements.

Gas/Plasma Cherenkov Radiation as a Diagnostic of Plasma Density

Emissions produced by the electron beam propagating partially ionized vapor of the Li oven have been measured near atomic spectral lines. The Cherenkov spatial profile has been studied as a function of oven temperature and pressure, observation wavelength, and ionizing laser intensity and delay. The Cherenkov peak angle is detected by the creation of plasma; estimates of plasma and neutral density have been extracted. Large increases in visible background radiation consistent with increased plasma recombination emissions due to dissipation of wake fields were simultaneously measured.

Transverse Betatron Dynamics of a 30GeV Beam in a Long Plasma

In the E-157 experiment, the electron beam is not matched to the plasma. As a consequence, the betatron motion of individual electrons produces multiple oscillations of the electron beam envelope over the plasma length, and the spot size of the beam downstream from the plasma varies with n_0 . Figure 2c shows the electron beam spot size σ_x measured at the downstream OTR as a function of the beam phase advance in the plasma. The line in Figure 2c is the solution to the beam envelope equation for a beam with a focus at the upstream UV pellicle (see Figure 1). The good agreement between the experimental data and the envelope equation solution for a beam in a pure ion channel confirms that the transverse wake fields are excited as expected from the PWFA theory in the “blow-out” regime.

In the case of a beam matched to the plasma ($\beta_{beam} = \beta_{plasma}$, as achievable at the IPO location), the beam spot size at the plasma exit remains constant ($\pm 2.5\%$) over a wide range of plasma densities (see Figure 6), and can be imaged on to the energy measurement plane, yielding a much larger n_0 range over which particles’ energy can be measured. In addition, the transverse momentum imparted to the beam tail by the plasma is expected to be much less than in the unmatched case.

Experimental Test for the Electron–Hose Instability

A beam with a longitudinal-transverse correlation (tilt), would experience a transverse instability known as the electron-hose instability. In analogy with a

quadrupole, any portion of the beam that is offset with respect to the center of the ion column will experience a dipole field linearly proportional to the offset, resulting in a beam tail oscillation with respect to the head of the beam. The linear theory of the electron-hose instability predicts that for the parameters of the E-157 (beam charge, bunch length, and plasma density) the amplitude of this oscillation will grow. Some data was analyzed to look for this instability. For these data the incoming beam has a tilt of $5.3\mu\text{m}/z$ at the entrance of the plasma (IP1). The beam centroid oscillates in the ion channel as expected from the envelope equation. Up to the maximum plasma density achieved, no growth of amplitude was measured.

High-Gradient Acceleration of Electrons in a Meter-Long Plasma Wakefield Accelerator

Time resolved energy spectra are obtained from streak camera images of the beam in the energy dispersive plane after the FFTB dipole dump magnet. For the analysis the beam image is cut in time slices of 1ps and the mean energy of each slice is calculated. A sample of this analysis for several events is shown in Figure 7a. In this example, the core of the beam lost an average of 30MeV while the electrons in the last tail slice gained an average of 120 MeV. A typical streak camera image obtained at the optimum plasma density is displayed in Figure 7b. This image again shows the same energy loss and gain in the beam slice centroids and also shows particles, appearing as single events on the image, accelerated to even higher energies. Without an imaging spectrometer these results are sensitive to the behavior of the beam tail. Thus, a good understanding of beam transverse dynamics is necessary for a complete understanding of the beam longitudinal dynamics.

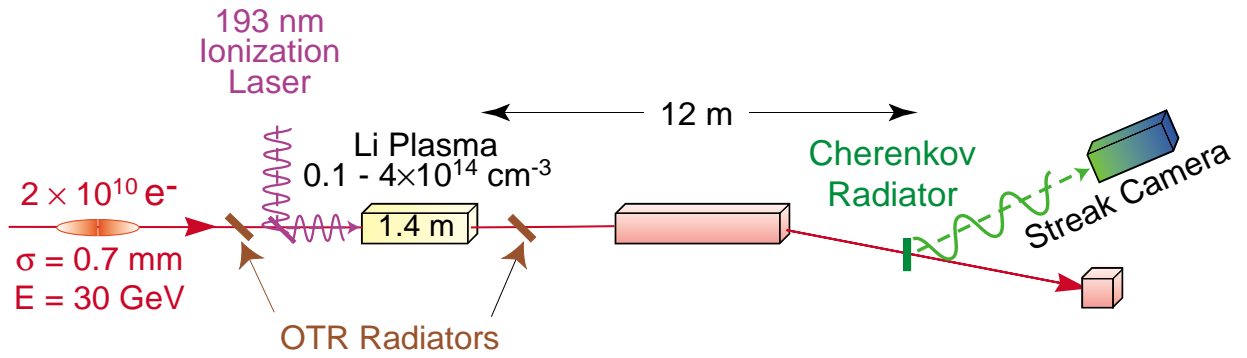


Figure 1: The E-157 experimental apparatus is shown schematically. 30 GeV electrons from the SLAC linac are transported through the FFTB to IP1 (Interaction Point 1) where the plasma is located. Beam profiles are measured before and after the plasma using optical transition radiation. The FFTB permanent magnet dump, which is almost immediately after the plasma, disperses the beam at a Cherenkov radiator at IP2, 12 m from the end of the plasma. The Cherenkov light is analyzed with a streak camera to give a measurement of energy vs. time in the bunch. The plasma is a 1.4 m long Lithium vapor that is partially ionized by a 193nm laser.

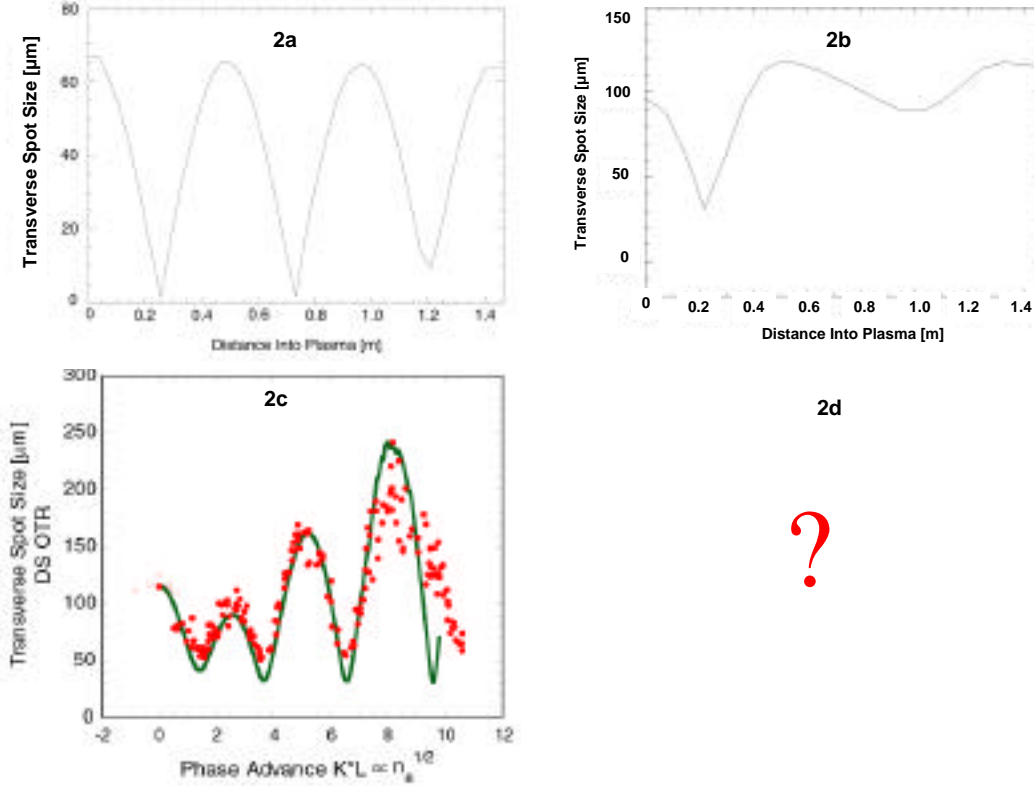


Figure 2: Transverse dynamics of electron and positron beams in a long plasma. 2a) Simulations showing the electron beam size oscillations within the 1.4 meter long plasma, 2b) Simulations for a positron beam in a homogeneous plasma analogous to the simulations for electrons shown in 2a, 2c) Beam spot size measured using OTR, about 1 m downstream from the plasma exit. Empty symbols correspond to plasma off. The line corresponds to the solution to the beam envelope equation for $\sigma_x=43 \mu\text{m}$ and $\epsilon_{nx}=9 \cdot 10^{-5} \text{ m-rad}$ ($\beta_x=1.3 \text{ m}$). 2d) Data to be taken during the first stage of the experimental program outlined in Section VI.

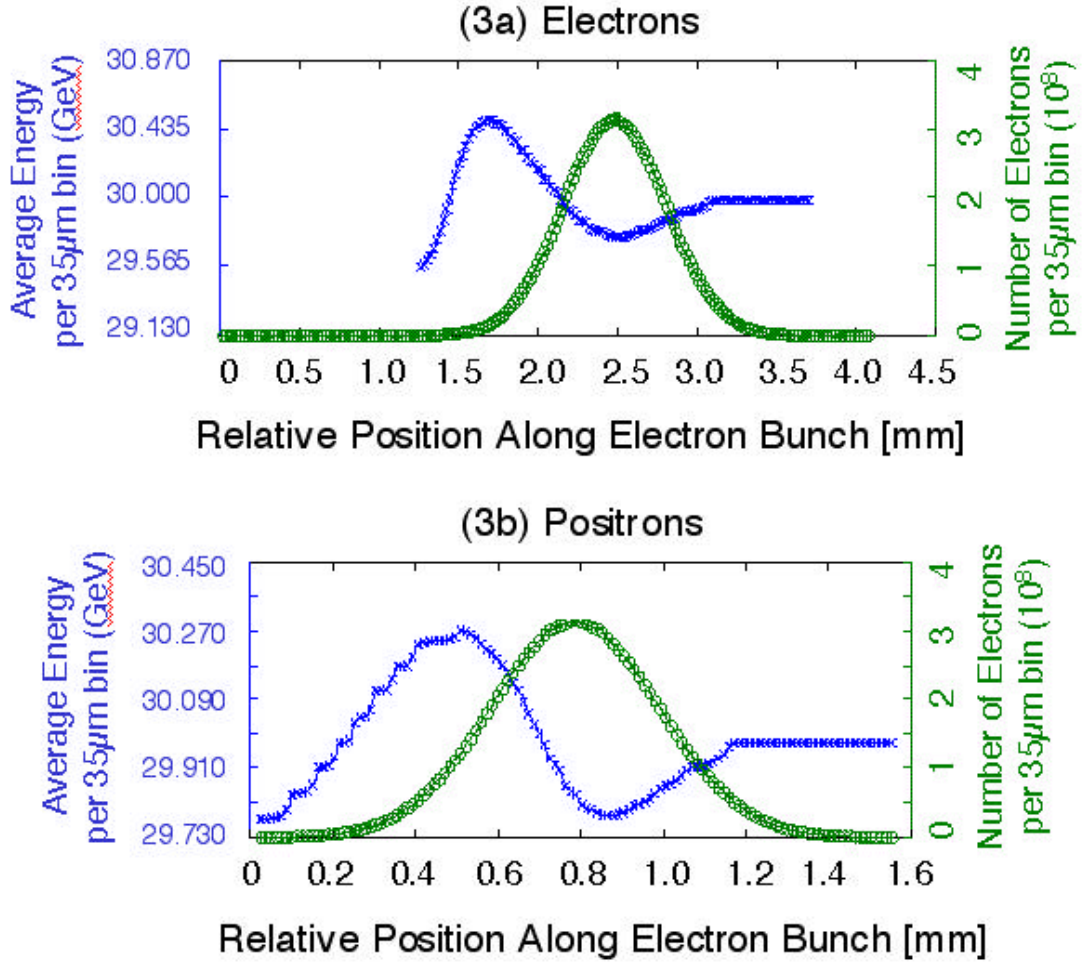


Figure 3: 3-D PIC simulations for a bunch of (a) electrons, and b) positrons) propagated roughly 1.6 cm into the plasma to let the longitudinal wakes develop. The accelerating gradients and an energy spectrum when extrapolated to 1.4m are shown along with the bunch distribution. Positrons in the maximum energy bin in the tail of the bunch have a bin-averaged gradient of 192 MeV/m. The electron-driven case with the same parameters shows a maximum bin-averaged gradient of 340 MeV/m. When scaled to a bunch length of 0.65mm, the gradients are correspondingly lower: 75 MeV/m for positrons and 130 MeV/m for electrons.

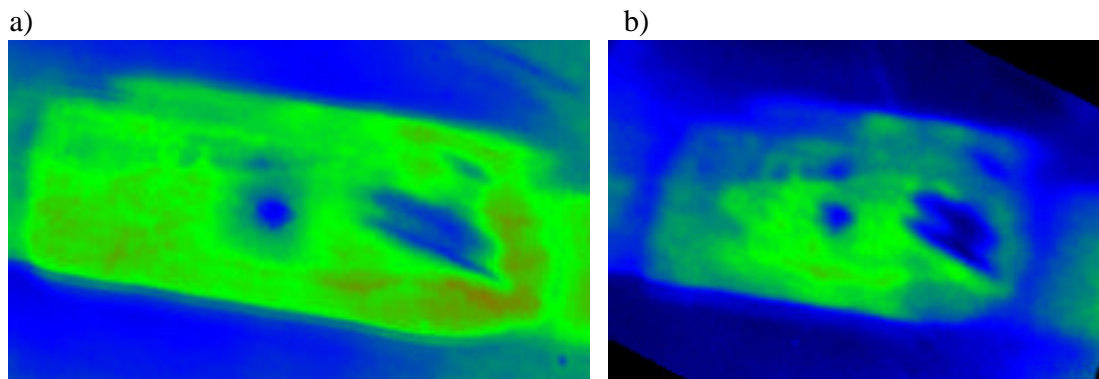


Figure 4: UV profiles 0.3 m (a) and 1.3 m (b) from a damaged UV optic with ~ 500 mm hole in reflective coating (center of images) as well as other forms of damage. The structure of the resultant mask in UV fluence is preserved over the required length to photo-ionize a hollow channel plasma.

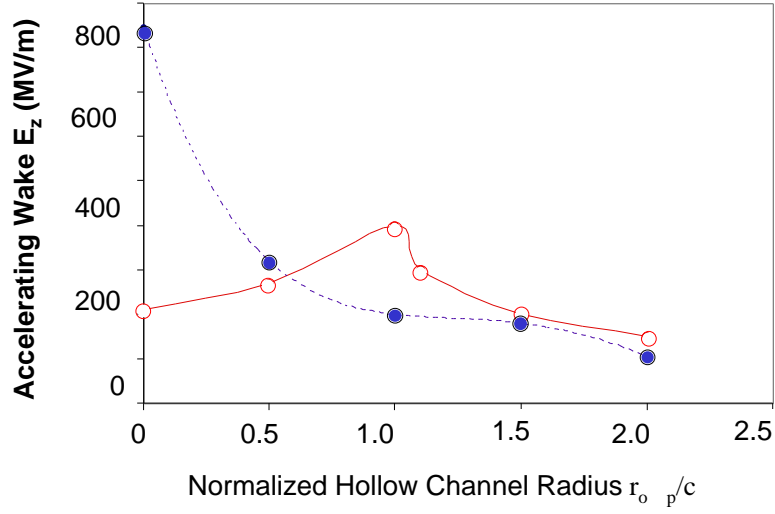


Figure 5: Accelerating wake for electron and positron beams as a function of the hollow plasma channel radius. For the electron case (filled blue circles) the wake amplitude decreases with channel radius, where as for positrons (open red circles) the wake has an maximum for a channel radius equal to c/ω_p .

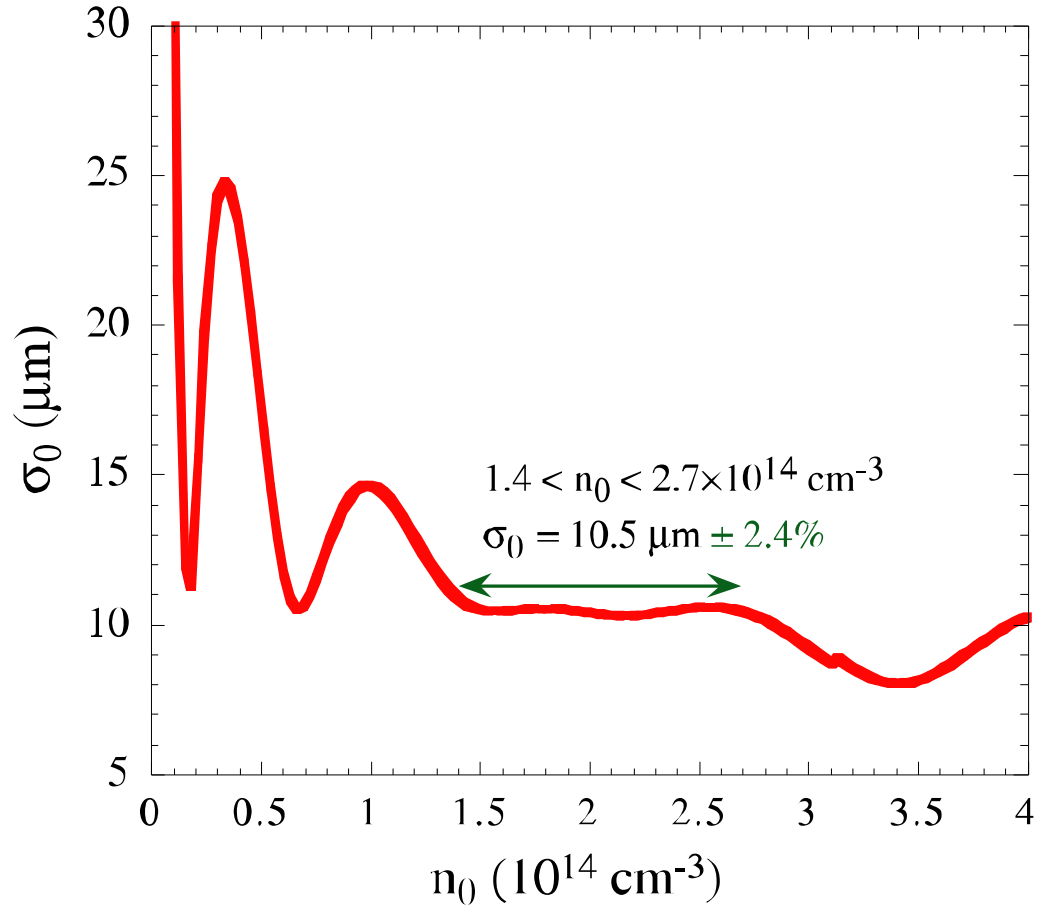


Figure 6: Beam spot size (σ_0) at the plasma exit calculated from the beam envelope equation for a beam matched to the plasma at $n_0 = 1.5 \times 10^{14} \text{ cm}^{-3}$: $\sigma = 10 \text{ } \mu\text{m}$, $\varepsilon_n = 5 \times 10^{-5} \text{ m rad}$, $\beta = 13 \text{ cm}$.

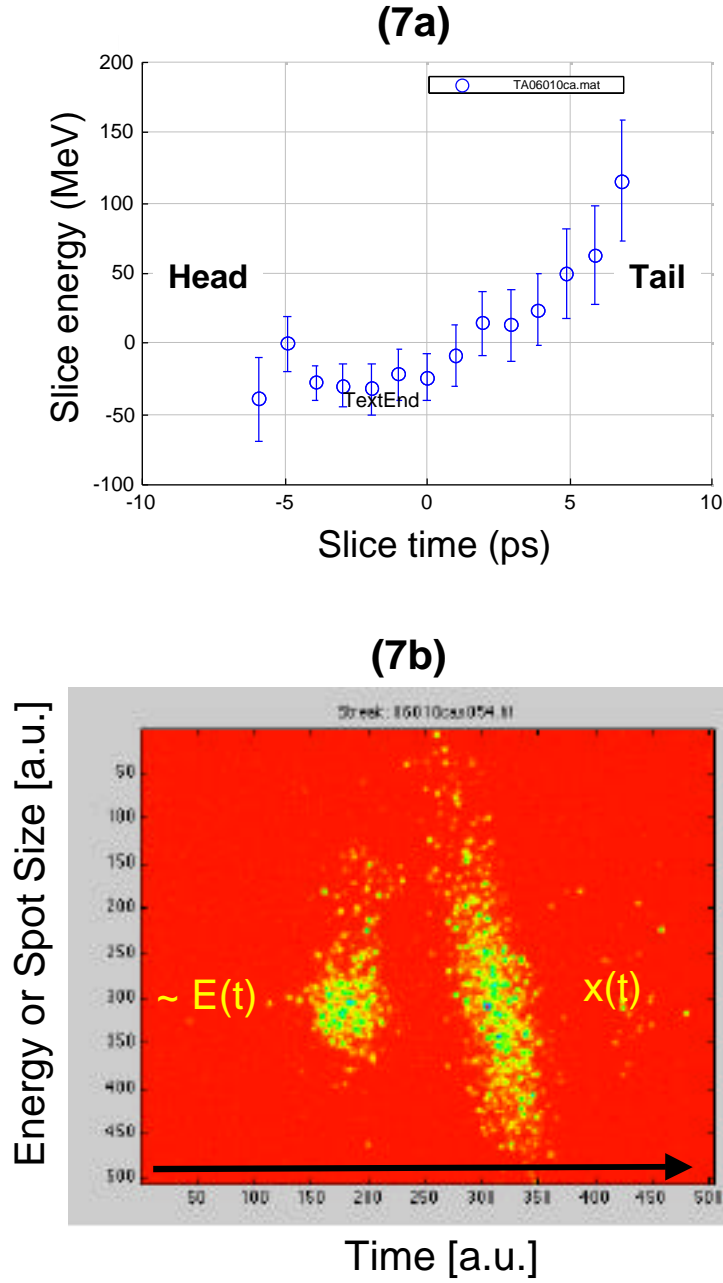


Figure 7: Time resolved energy spectra of the beam for a) multiple events and b) a single event. The average energy loss for the several events in a) is around 30MeV while the average energy gain for particles furthest in the tail is around 120MeV. The single event shown in b) indicates that particles are accelerated to energies higher than the slice average energy.

Appendix I

Dynamic effects in plasma wakefield excitation

R. G. Hemker, W. B. Mori, S. Lee, and T. Katsouleas

Physical Review Special Topics – Accelerators and Beams **3**, 061301 (2000)

Dynamic effects in plasma wakefield excitation

R. G. Hemker and W. B. Mori

Department of Physics and Astronomy, University of California at Los Angeles, Los Angeles, California 90095-1547

S. Lee and T. Katsouleas

Department of Electrical Engineering, University of Southern California, Los Angeles, California 90089-0271

(Received 2 December 1999; published 26 June 2000)

We have used 2D cylindrically symmetric particle-in-cell simulations to investigate the dynamics of a high energy electron beam propagating through an underdense plasma. The simulation parameters are relevant to a recent plasma wakefield experiment conducted at the Stanford Linear Accelerator Center [R. Assmann *et al.*, Stanford Linear Accelerator Center Proposal, 1997]. We model the dynamic development of the beam and wakefield excitation over meters of propagation length. To most clearly illustrate the dynamics of both the beam and the wakefield, a video of the simulation data is presented. The main observation is that the beam dynamics, i.e., its betatron motion in the resulting ion channel, agree well with the theoretical predictions while the plasma wake remains almost invariant over the entire propagation distance. The video illustrates subtle details regarding the interplay between the beam dynamics and wakefield generation. The results presented here complement results published separately [S. Lee *et al.*, Phys. Rev. E **61**, 7014 (2000)].

PACS numbers: 52.65.Rr, 52.40.Mj, 41.75.-i

I. INTRODUCTION

The basic concept of a plasma wakefield accelerator (PWFA) is to accelerate a low current trailing electron bunch by the wakefield generated by a high current driver [1,2]. If the driving bunch is highly relativistic, then both the accelerating as well as the accelerated bunch are moving with about the speed of light and the accelerated bunch can stay in phase with the accelerating field for distances long enough to gain significant amounts of energy. Motivated by and as part of the preparations for an experiment which was recently conducted at the Stanford Linear Accelerator Center (SLAC), we have simulated a plasma wakefield accelerator with the expected parameters of this experiment [3]. In this experiment a 30 GeV electron beam at SLAC is used to excite a wake of the order of 1 GeV/m in a 1.4 m long plasma of density $1\text{--}2 \times 10^{14} \text{ cm}^{-3}$. In this wake the centroid energy of the tail of the beam is expected to increase by several hundred MeV. Since the beam in this experiment is typically much denser than the plasma (e.g., $N = 3.5\text{--}4 \times 10^{10}$ electrons in a $\sigma_z = 0.6$ mm bunch length and a spot size of $\sigma_r = 50 \text{ }\mu\text{m}$ corresponding to a beam density $n_b = 1 \times 10^{15} \text{ cm}^{-3}$), the PWFA is in the highly nonlinear or so-called blowout regime [4]. The advantages that this regime offers are a high accelerating gradient, a constant accelerating structure with respect to the transverse dimensions, a linear focusing force, and a high transformer ratio. However, in this nonlinear regime, linear theory or fluid models are inapplicable and do not provide an accurate understanding of the physics. Much better insight into the physical processes can be gained by using particle-in-cell (PIC) simulations, which allow ac-

curate modeling of highly nonlinear processes such as the ones occurring here. For these reasons, we conducted PIC simulations to investigate this regime of plasma wakefield acceleration. Many of these results can be found elsewhere [5]. In this paper we provide more detail on the dynamics of the drive beam and wakefield evolution. The presentation is aided through simulation generated videos.

II. SIMULATION SETUP AND RESULTS

We carried out simulations for the physical parameters similar to the ones described above using the newly developed, object-oriented, parallel PIC code OSIRIS [6]. This PIC code is fully explicit and therefore contains all of the relevant physics. Because of its object-oriented structure, this code contains algorithms for several geometries and dimensions as well as current deposition schemes. The algorithms for the results presented in this paper were 2D cylindrically symmetric, and a rigorously charge conserving current-deposition algorithm was used [7]. The code also uses a moving simulation window [8], which moves at the speed of light, i.e., with the beam. This limits the simulation domain to the beam and its immediate surroundings rather than the whole propagation distance of the beam. The simulation window in normalized units had a size along the propagation direction z of $25c/\omega_p$ and a size in the radial direction r of $10c/\omega_p$ with a grid of $N_z \times N_r = 500 \times 200$. Here c is the speed of light and ω_p is the plasma frequency for a given plasma density n_p . We will use $n_p = 2.1 \times 10^{14} \text{ cm}^{-3}$, which corresponds to $c/\omega_p = 0.367 \text{ mm}$, throughout this paper when converting simulation results back into physical units.

This means the simulation window corresponds to a size of $9.175 \text{ mm} \times 3.67 \text{ mm}$. The beam propagated through the plasma for 190 000 time steps with $dt = 0.02\omega_p^{-1}$ (corresponding to $18.35 \mu\text{m}$ of propagation distance per time step) for a total of $3800c/\omega_p$ ($\sim 1.4 \text{ m}$). Nine particles per cell were used for the background plasma and 25 particles per cell for the beam. The beam's longitudinal profile was fitted to the experimentally known profile of the SLAC beam [3], which is very close to a Gaussian profile of width $\sigma_z = 0.63 \text{ mm}$, and transversely as a Gaussian of width $\sigma_r = 70 \mu\text{m}$. The peak density was taken to be $7.56 \times 10^{14} \text{ cm}^{-3}$. Therefore the simulated electron bunch contained 3.7×10^{10} electrons.

Figures 1(a) and 1(b) show the first and the last frames of the video accompanying this paper. The video shows seven different aspects of the simulation data. In the upper left-hand corner is a colored, rubber sheet representation of the longitudinal, accelerating electric field. For

this visualization the elevation of a surface point as well as its color represent the field strengths of the electric field. Note that we chose a perspective for visualizing the rubber sheet surface so that negative field values of the electric field would be represented by positive values of the surface elevation. This leads to a better visualization of the accelerating region. The sharp edge of the rubber sheet surface going roughly from the upper left-hand corner to the lower right-hand corner is due to the axial boundary of the 2D cylindrically symmetric simulation and, accordingly, r increases starting from this axial boundary toward the lower left-hand corner. Because of the chosen perspective, the rubber sheet does not show the data for the whole simulation. The upper middle of the video frame shows the value of the longitudinal electric field along the axial boundary for its full length of $25c/\omega_p$. The figure in the lower middle below the electric field lineout shows the energy gain and loss of the

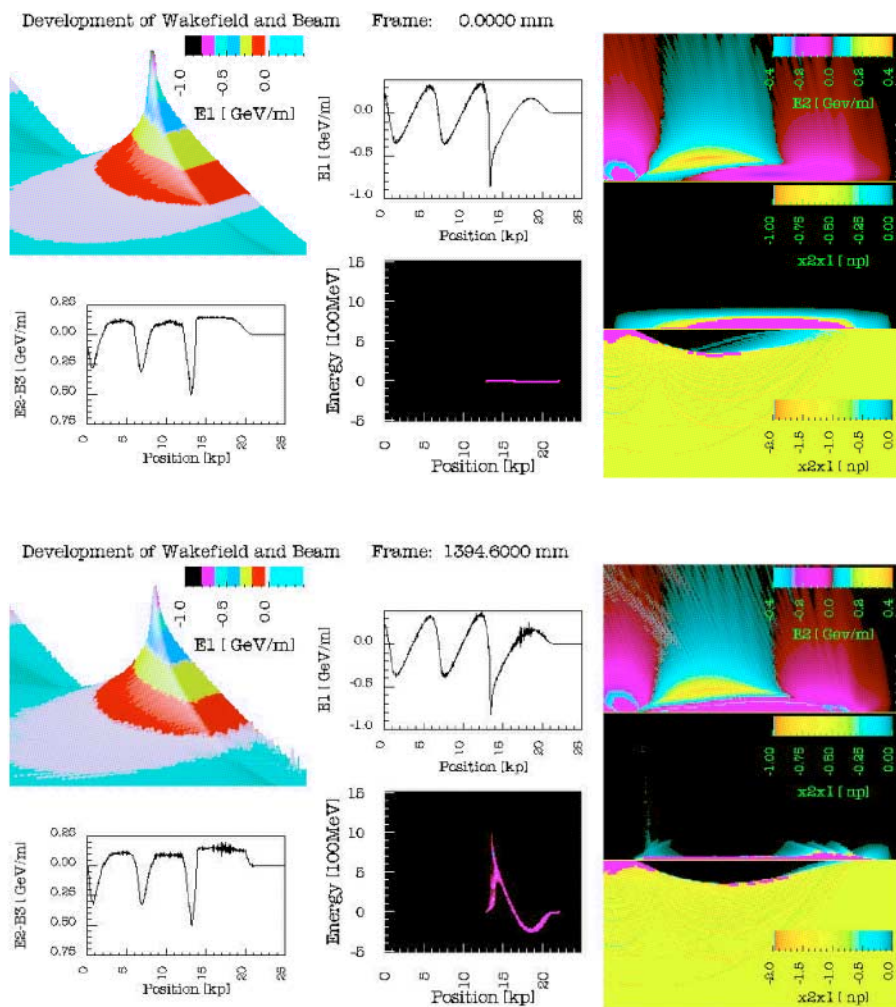


FIG. 1. (Video) The first and the last frames of the video accompanying this paper. The different plots of the video are (column by column from the top to the bottom) E_z : rubber sheet; $E_r - B_\theta$: focusing field lineout σ_r off axis; E_z : lineout on axis, beam-energy change as a function of $z-ct$; E_r in the $r-z$ plane; n_{beam} in the $r-z$ plane; n_{plasma} in the $r-z$ plane (direction of r reversed). Please note that in the figures and the video the indices 1, 2, and 3 are used instead of z , r , and θ .

electron beam as a function of the axial position. The colored areas indicate the parts of this plot where beam electrons are present. Note that the horizontal axis of this plot is precisely aligned with the axis of the field lineout above. The plot in the lower left-hand corner shows the focusing field experienced by the beam electrons, $E_r - B_\theta$, at a position $73.4 \mu\text{m} \equiv \sigma_r$ off axis. The right-hand column shows three color plots in the r - z plane (in the video frame also labeled as the x_2 - x_1 plane). The plots shown (from top to bottom) are the radial electric field E_r , the charge density of the beam, and the charge density of the background plasma. This last plot has been mirrored along the axis to allow for a more direct comparison of the plasma density with the beam density. The horizontal axis for each of the three plots goes from 12.5 to $22.5c/\omega_p$ of the simulation window and the vertical axis shows 0 to $5c/\omega_p$ along the radial direction. The field and density values are given by the color bars in each of the plots. Note that the areas of the plots colored in magenta are areas in which the field or density values are outside the respective color scales. Since the color code of the beam charge density plot reaches from 0 to 1 , which is the normalized density of the background plasma, the magenta-colored areas in this plot indicate densities above the background plasma density.

The video consists of a total of 191 frames at a speed of 10 frames/sec. With such a large number of frames the video can clearly illustrate subtle points in the evolution of the beam and wake. The first fact to note when watching the video is the lack of change over time in the evolution of the accelerating electric field and the focusing field. With the exception of the peak accelerating field, which fluctuates slightly by about ± 0.05 GeV/m around a value of about 0.75 GeV/m (about $\pm 7\%$), and some slight variation in the level of numerical noise, the accelerating electric field essentially does not change over time. This is in strong contrast to the dynamic development of the beam radius (middle plot in the right-hand column) and energy (lower plot in the center column) and the radial electric field (upper plot in the right-hand column). The energy plot shows that every part of the beam except the front part and the very tail gains or loses energy linearly as a function of time. This is consistent with the constant longitudinal field since at an initial energy of about 30 GeV the beam electrons experience no significant phase slippage over the time of the simulation.

Two other effects can also be observed. First, there is a slight broadening of the front part of the decelerated area of the beam along the energy axis, which means that not all electrons at a given z experience exactly the same decelerating field. Second, there is a large energy spread of the very back of the beam tail, which splits into two parts. The first observation can be understood when looking at the background plasma charge density. The plasma charge density plot shows that in the front part of the beam the area of total electron blowout is smaller than

in the latter parts of the beam, and therefore the radius up to which the focusing force F_r is independent of z is smaller. According to the Panofsky-Wenzel theorem, $\partial F_r / \partial z = \partial F_z / \partial r$, this implies an acceleration gradient that varies along the radial position [4]. This can also be noticed for the region of decelerating field that is visible in the lower right-hand corner of the E_z rubber sheet plot. The radially flat area increases slightly in width toward the back. The broadening of the front part of the deceleration area of the beam is a result of this nonuniform accelerating field. The energy spread of the tail of the beam can be understood by looking at the narrowing of the accelerating and focusing field profile near the peak accelerating field. It shows that a part of the tail of the beam, in contrast to the rest of the beam, experiences a strong defocusing force that pushes it radially out of the accelerating field. The blowout of some of the tail electrons of the beam can also be seen in the development of the beam charge density.

The evolution of the main part of the beam, as seen in the beam charge density plot, is clearly dominated by the betatron oscillation of the beam in the focusing field. The focusing field is mainly due to the ions left in the plasma blowout area, as seen in the plasma charge density plot, since the effects of electric and magnetic fields of the relativistic beam on itself cancel each other almost completely. The linear focusing force in the blowout area results in the same oscillation frequency for all beam electrons in that area. The beam propagates while undergoing betatron oscillations with a wavelength of the spot size

$$\lambda_{\text{spot size}} = \lambda_\beta / 2 = \pi \sqrt{\frac{\gamma m c^2}{2\pi e^2 n_0}}, \quad (1)$$

where λ_β is the betatron wavelength of a single particle. Measuring this wavelength using the minima of the oscillation of the beam density gives a wavelength $\lambda_\beta / 2 = 40$ cm as predicted by Eq. (1) for the density of the simulation [3].

The dynamics of the front part of the beam is more complex because the blowout area there is not as wide. This leads to nonharmonic oscillations or so-called aberrations in the focusing force, which leads to phase mixing of the electrons. The oscillation frequency of the beam electrons decreases toward the front. The video shows clearly that after the main part of the beam reaches an oscillation minimum this minimum moves forward toward the front of the beam as the electrons there execute betatron oscillations with lower frequencies. This dynamics at the front of the beam leads to a subtle point, which was not appreciated until the video was made. Namely, the focusing field for the beam, $E_r - B_\theta$, shows an unexpected behavior with time. Initially the focusing force rises slowly over the first one-fourth of the beam, but once the head of the beam begins to pinch the rise becomes steeper. The

unexpected behavior results because the transverse profile never relaxes back to the original one. Instead, there is always an axial slice of the beam at the head of the beam that is near a pinch. So on average, the beam density at the front of the beam is always larger than it was at $t = 0$. As a result, the occurrence of complete blowout is earlier in the beam and the region of blowout is wider leading to more of the beam undergoing the uniform betatron oscillations than might have been expected.

Unlike the beam, the plasma electrons respond predominantly to only E_r . Thus, the blowout of the plasma electrons and their oscillation back onto the axis in the back of the pulse is caused by the total radial electric field that they experience. The video shows that the radial field has two distinct regions. The front, where the plasma electrons are not blown out yet, is dominated by the electric field of the beam; the back, where the plasma electrons are blown out, is dominated by the radial electric field of the remaining ion charge. The plasma charge density plot shows the effect of this. In the moving window frame, i.e., in the z - ct coordinate, the plasma electrons stream backward past the stationary drive beam. After the radial field force deflects the electrons outward, most of them coalesce in a narrow, high density surface layer that lies at the edge of the blowout region. The radius of the blowout region [5], and therefore the radial position of the layer, is roughly $2\sigma_r\sqrt{n_b/n_0}$. The electrons stream backward within this narrow surface layer and converge on the axis creating a very dense spike and, therefore, a sharp peak in the accelerating field. (Note that in the laboratory frame individual electrons are blown out and then return while remaining near their initial z value, but we will use the moving window point of view for its convenience of description.) The insensitivity of the accelerating wakefield to the dynamic beam development is a consequence of the beam being narrow when compared to the radius at which the surface layer is located. For most of the plasma oscillation, all of the plasma electrons are outside of the beam so that from Gauss law the electrostatic field affecting them is independent of the radius of the charge inside. Thus the betatron pinching of the beam has little effect on the plasma electrons and hence the wake. The slower evolution in the front of the beam does not have any significant effect either since the slight variations in the initial trajectories of electrons become insignificant after the blown out electrons reach the surface layer. The surface layer is shown in Fig. 2, where a radial lineout of the plasma charge density at the center of the beam is plotted after 1.4 m of propagation. The plasma blowout as well as the surface layer are clearly visible.

Because of the invariance of the accelerating field, the expected energy gain can be predicted with confidence for a specified beam charge and profile. The longitudinal momentum p_z ($\cong \gamma$) versus ct phase space is shown in Fig. 3 to illustrate the expected acceleration of the beam

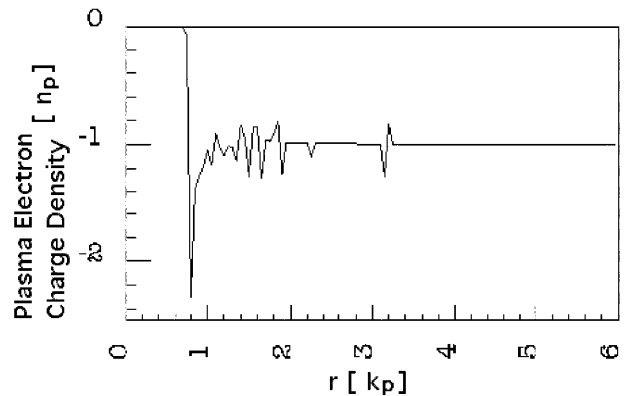


FIG. 2. A radial lineout of the background plasma electron charge density at the center of the beam after 1.4 m of propagation.

after 1.4 m of propagation. The mean, maximum, and minimum energy of the beam are plotted in 0.12 psec bins along the length of the beam [Fig. 3(a)]. This is done in Fig. 3(a) for the actual simulation particle data after 1.4 m. Figure 3(b), by contrast, was generated by using the initial particle data propagated for 1.4 m using the initial fields at the initial positions of the particles. This makes the assumption of a nonevolving field and neglects the betatron oscillation of each particle. The mean, maximum, and minimum energies resulting from these two graphs are very similar for most of the beam. The results differ only at the very end of the beam where Fig. 3(b) shows larger average and maximum energies and lower minimum energies than Fig. 3(a). The similarity between the two figures for the main part of the beam is consistent with our assumption of nonevolving wakefield if the accelerating field has a constant value within the radial range of the betatron oscillation for each particle. The differences in the tail are due to the fact that the particles in the tail at larger radii do not experience a constant accelerating field during their radial motion. For the full simulation this leads to an averaging out of the different accelerations experienced by each particle due to its transverse motion. For the particles accelerated with the initial field this averaging does not happen and the maximum and minimum energies in the beam tail of Fig. 3(b) are therefore a measure of the maximum and minimum accelerating field in that part of the wake. Based on these figures we can say that the maximum field is about 0.85 GeV/m but that the maximum energy gain by a particle after 1.4 m will be about 1 GeV. The maximum mean energy for a 0.12 psec bin is 550 MeV with about 7×10^7 electrons in this maximum energy bin. This is again consistent with the information in the video for these numbers. The conclusion from Figs. 3(a) and 3(b) is that the betatron oscillations do not have a significant influence on the acceleration of the beam.

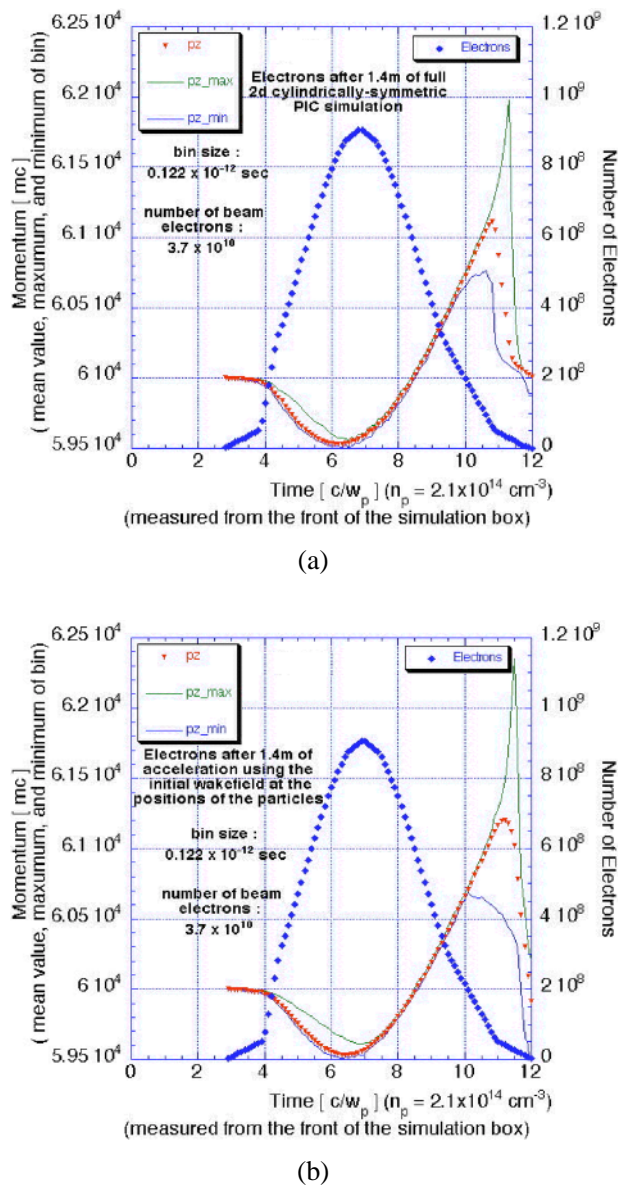


FIG. 3. (Color) The mean, maximum, and minimum energy as well as the number of electrons for each 0.12 psec bin after 1.4 m of propagation using (a) the full PIC simulation and (b) the initial fields at the initial positions of the particles to propagate the beam

III. CONCLUSIONS

The main result of the analysis of the beam and wakefield dynamics is that the wakefield is rather insensitive to the betatron oscillation dynamics of the beam and therefore essentially constant over time. In addition, the acceleration and deceleration of the beam electrons is also not affected by the betatron oscillation either. The blowout

regime therefore provides a stable and robust plasma wakefield acceleration. Energy gains on the order of GeV should be achievable in this blowout regime if the physical parameters of the simulations can be realized in an experiment. Far higher gradients and energy gains may be possible with shorter bunches and longer denser plasmas [3]. Such beams would undergo hundreds rather than a few betatron oscillations. Although it may be desirable to match the beam emittance to the plasma focusing strength to avoid betatron oscillations as discussed in Ref. [3], the analysis here suggests that the presence of the oscillation is not necessarily detrimental. A major issue on the scaling of scaling plasma wakefield acceleration to the 10 and 100 s of GeV is the possibility of a hosing instability of the beam [9], which might reduce the achievable energy gain and lead to emittance growth of beam. Hosing is inherently a 3D instability and is therefore absent in these 2D simulations. We are currently carrying out 3D simulations to study the importance of hosing and other 3D effects.

ACKNOWLEDGMENTS

We acknowledge useful conversations with the entire E-157 Collaborative Team. This work is supported by DOE Contracts No. DE-FG03-92ER40727, No. DE-FG03-98DP00211, and No. DE-FG03-92ER40745, NSF Grant No. DMS-9722121, and LLNL Contract No. W-7405-ENG-48.

- [1] P. Chen, J.M. Dawson, R.W. Huff, and T. Katsouleas, Phys. Rev. Lett. **54**, 693 (1985).
- [2] E. Esarey, P. Sprangle, J. Krall, and A. Ting, IEEE Trans. Plasma Sci. **24**, 252 (1996).
- [3] R. Assmann *et al.*, Stanford Linear Accelerator Center Proposal, 1997.
- [4] J.B. Rosenzweig, B. Breizman, T. Katsouleas, and J.J. Su, Phys. Rev. A **44**, R6189–R6192 (1991).
- [5] S. Lee, T. Katsouleas, R.G. Hemker, and W.B. Mori, Phys. Rev. E **61**, 7014 (2000).
- [6] R.G. Hemker, F.S. Tsung, V.K. Decyk, W.B. Mori, S. Lee, and T. Katsouleas, in *Proceedings of the 1999 Particle Accelerator Conference, New York* (IEEE, Piscataway, NJ, 1999).
- [7] J. Villaseñor, Comput. Phys. Commun. **69**, 306–316 (1992).
- [8] K.C. Tzeng, W.B. Mori, and C.D. Decker, Phys. Rev. Lett. **76**, 3332 (1996).
- [9] D.H. Whittum, W.M. Sharp, S.S. Yu, M. Lampe, and G. Joyce, Phys. Rev. Lett. **67**, 991 (1991).

Appendix II

E-157: A 1.4-m-long plasma wake field acceleration experiment using a 30 GeV electron beam from the Stanford Linear Accelerator Center Linac

M. J. Hogan, R. Assmann, F.-J. Decker, R. Iverson, P. Raimondi, S. Rokni, R. H. Siemann, D. Walz, D. Whittum, B. Blue, C. E. Clayton, E. Dodd, R. Hemker, C. Joshi, K. A. Marsh, W. B. Mori, S. Wang, T. Katsouleas, S. Lee, P. Muggli, P. Catravas, S. Chattopadhyay, E. Esarey, W. P. Leemans
et al.

Physics of Plasmas 7, 2241 (2000)

E-157: A 1.4-m-long plasma wake field acceleration experiment using a 30 GeV electron beam from the Stanford Linear Accelerator Center Linac*

M. J. Hogan,[†] R. Assmann,^{a)} F.-J. Decker, R. Iverson, P. Raimondi, S. Rokni, R. H. Siemann, D. Walz, and D. Whittum

Stanford Linear Accelerator Center, Stanford University, Stanford, California 94309

B. Blue, C. E. Clayton, E. Dodd, R. Hemker, C. Joshi, K. A. Marsh, W. B. Mori, and S. Wang

University of California at Los Angeles, Los Angeles, California 90095

T. Katsouleas, S. Lee, and P. Muggli

University of Southern California, Los Angeles, California 90089

P. Catravas, S. Chattopadhyay, E. Esarey, and W. P. Leemans

Lawrence Berkeley National Laboratory, Berkeley, California 94720

(Received 22 November 1999; accepted 24 January 2000)

In the E-157 experiment now being conducted at the Stanford Linear Accelerator Center, a 30 GeV electron beam of 2×10^{10} electrons in a 0.65-mm-long bunch is propagated through a 1.4-m-long lithium plasma of density up to $2 \times 10^{14} \text{ e}^-/\text{cm}^3$. The initial beam density is greater than the plasma density, and the head of the bunch expels the plasma electrons leaving behind a uniform ion channel with transverse focusing fields of up to several thousand tesla per meter. The initial transverse beam size with $\sigma = 50\text{--}100 \mu\text{m}$ is larger than the matched size of $5 \mu\text{m}$ resulting in up to three beam envelope oscillations within the plasma. Time integrated optical transition radiation is used to study the transverse beam profile immediately before and after the plasma and to characterize the transverse beam dynamics as a function of plasma density. The head of the bunch deposits energy into plasma wakes, resulting in longitudinal accelerating fields which are witnessed by the tail of the same bunch. A time-resolved Cherenkov imaging system is located in an energy dispersive plane downstream of the plasma. It images the beam onto a streak camera allowing time-resolved measurements of the beam energy spectrum as a function of plasma density. Preliminary experimental data from the first three runs are compared to theory and computer simulations.

© 2000 American Institute of Physics. [S1070-664X(00)97805-4]

I. INTRODUCTION

Plasma-based acceleration schemes¹ utilizing relativistically propagating plasma waves have been under active investigation because of their potential to accelerate charged particles at gradients that are orders of magnitude greater than those currently employed in rf cavities. Specifically, such relativistic plasma waves are excited by using either laser pulses² or short electron bunches.³ Both techniques have shown acceleration of electrons in proof-of-principle experiments.⁴ Laser-driven schemes such as the beat-wave accelerator,⁵ the laser-wake field accelerator,⁶ and the self-modulated wake field accelerator⁷ have accelerated electrons with impressive gradients, much in excess of 1 GeV/m, but over rather small ($<1 \text{ cm}$) distances. Consequently, the energy gains have been $\leq 100 \text{ MeV}$.⁸ An electron beam-driven plasma wake field accelerator (PWFA)⁹ has accelerated electrons over a longer length ($\sim 30 \text{ cm}$) but at a much smaller

gradient ($\leq 50 \text{ MeV/m}$). This is mainly due to the limit on the total charge and length of the drive electron bunch. If plasma-based accelerators are to have any relevance to future high energy colliders it is essential to show high-gradient ($\geq 100 \text{ MeV/m}$) acceleration over a long distance.

The purpose of the present experiment is to demonstrate acceleration of electrons by plasma wake field acceleration with gradients in excess of 100 MeV/m over a distance greater than 1 m. The experiment called E-157¹⁰ and described in this paper, is ongoing at the Final Focus Test Beam facility (FFTB) at the Stanford Linear Accelerator Center (SLAC). It is carried out by a multi-institution collaboration involving Lawrence Berkeley National Laboratory (LBNL), SLAC, the University of California at Los Angeles (UCLA), and the University of Southern California (USC).

The experiment uses a high peak-current ($>100 \text{ A}$), ultrarelativistic ($\gamma \gg 1$) electron bunch from the Stanford Linear Collider to access the so-called under-dense (or “blow-out”) regime of PWFA.¹¹ In this regime the drive electron-bunch density n_b exceeds that of the plasma density n_p . The plasma electrons are expelled by the space charge of the electron bunch leaving behind an ion channel which, ideally,

*Paper JI26 Bull. Am. Phys. Soc. **44**, 163 (1999).

[†]Invited speaker.

^{a)}Present address: European Organization for Nuclear Research (CERN), Geneva, Switzerland.

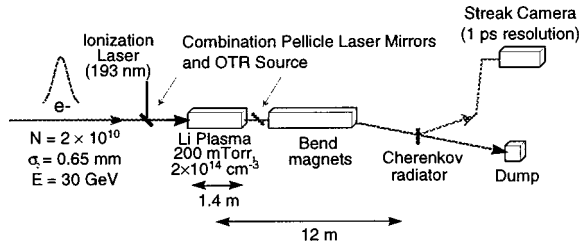


FIG. 1. The E-157 experiment is shown schematically: A 30 GeV electron bunch from the SLAC linac is propagated through a 1.4-m-long photoionized Li plasma of density up to $2 \times 10^{14} \text{ e}^-/\text{cm}^3$. The bunch exits the plasma and is dispersed by a dipole magnet. A Cherenkov imaging system in the dispersive plane images the beam onto the slit of a streak camera to resolve the beam energy and energy spread as a function of time.

provides a uniform (along the direction of propagation of the beam), and linear (in the transverse direction) focusing force on the beam. The plasma electrons then rush back into the ion channel to produce “an accelerating bucket” or a longitudinal wake field that can accelerate electrons in the tail of the drive bunch.

For the beam and plasma parameters of our experiment there are several distinct experimental observable in addition to the acceleration of electrons in the tail of the drive bunch. First, for a given length of plasma, the electron beam can undergo several betatron oscillations once the ion channel is established. These produce plasma density dependent oscillations of the electron beam spot size downstream of the plasma. Second, during the rise time of the electron bunch, while the ion channel is being formed, different longitudinal parts of the beam will undergo different betatron phase advances. This manifests itself as time-dependent focusing of the beam. Third, if there is a head-to-tail offset or tilt to the drive beam, the tail of the beam could oscillate due to the transverse wake fields (or focusing force) and even grow in amplitude due to the hosing instability.¹² Fourth, the bulk of the beam will experience an energy loss when creating the wake. All these effects produce characteristic experimental signatures and have to be quantified in order to clearly isolate the energy gain. This paper describes the current progress toward understanding these related effects.

II. EXPERIMENTAL APPARATUS

The bulk of the experimental apparatus is located in the FFTB at the end of the SLAC linac. The principal elements are the lithium plasma source, integrated mirrors and optical transition radiation (OTR) radiators, and finally an aerogel Cherenkov radiator located in the energy dispersive region downstream of the plasma. The experiment is shown schematically in Fig. 1.

A. Electron beam

The SLAC linac delivers a single electron bunch to the plasma at a rate of either 1 or 10 Hz. The electron beam diagnostics include toroidal current transformers for measuring the beam charge, beam position monitors, for measuring beam centroids and charge, wire scanners for measuring the average transverse beam size and its emittance, and disper-

TABLE I. Nominal electron beam and plasma parameters.

Parameter	Value
Electron Beam	
Number of electrons (N_e)	2×10^{10}
Energy (E)	30 GeV
Energy spread—uncorrelated	0.3%
Energy spread—correlated	Variable to 1%
Bunch length (σ_z)	0.65 mm
Horizontal spot size (σ_x)	50–100 μm
Vertical spot size (σ_y)	50–100 μm
Normalized x emittance (ϵ_x)	60 mm mrad
Normalized y emittance (ϵ_y)	8 mm mrad
Repetition rate	1 or 10 Hz
Plasma	
Plasma length	1.4 m
Plasma density (e^-/cm^3)	$< 2 \times 10^{14}$
Fractional ionization	$\sim 10\%$

sive regions for measuring the beam energy spectrum. Typical electron beam and plasma parameters are given in Table I.

Transverse wake fields in the accelerator rf structures can produce head–tail tilts and tail offsets that could lead to false energy gain signatures or no energy gain at all. Thus the setup of the linac upstream of the plasma is critical.¹⁰

The SLAC linac is currently configured for operation of the positron–electron storage ring PEP-II.¹³ Its impact on E-157 is briefly explored. The electron beam is accelerated up to ~ 30 GeV in the first two-thirds of the linac for positron production. The rf in the last third of the linac is mostly off. The rf has two principal functions: energy gain and manipulation of the correlated energy spread on the beam to control wake fields—so called BNS damping.¹⁴ No BNS damping in the last third of the linac leads to emittance growth and jitter amplification to unacceptable levels. If the energy spread of the beam is not removed prior to the end of the linac, BNS damping controls the wake fields and beam jitter, but the energy spread leads to chromatic effects in the FFTB. In practice the linac is setup to compromise between these two extremes.

Because of transverse wake fields the beam can have a head–tail offset on the order of tens of microns. Because the tail is offset with respect to the head of the beam, it is offset with respect to the center of the plasma focusing channel (which can be thought of as a quadrupole focusing in both planes) and receives a wake-field-like deflection. The focusing strength K_r (T/m) for a uniform ion column of density n_0 (cm^{-3}) is approximated by

$$K_r = 960\pi \frac{n_0}{10^{14}}.$$

For a plasma density of $2 \times 10^{14} \text{ cm}^{-3}$ and focusing gradients on the order of 6000 T/m, a 10 μm offset per longitudinal beam size σ_z can lead to a 2 mm deflection in the dispersive plane downstream at the Cherenkov radiator (see Fig. 1). This effect can in principle be quantified and subtracted from the energy measurement.

Head-tail effects are dependent on the betatron phase advance through the plasma. When the plasma density-length product is adjusted to correspond to a betatron phase advance equal to an integer multiple of π , the plasma is effectively transparent to the initial transverse beam distribution. When the betatron phase advance is an even multiple of π a particle will exit at its initial transverse position and angle, regardless of its incoming offset with respect to the center of the ion channel. When the betatron phase advance in the plasma is an odd multiple of π the tail will exit at a transverse position and angle opposite its initial position and angle. By adjusting the plasma density to an odd or even multiple of π the tail is either flipped in sign or not changed at all. When operating at this transparency condition, and given the dispersion of 0.085 m, a 10 μm tail offset would correspond to an apparent energy change of only ~ 3 MeV. Complications to this simple picture are discussed in Sec. III.

B. Plasma source

Given the drive beam parameters of Sec. II A, the plasma wavelength

$$\lambda_p(\text{cm}) = \frac{2\pi c}{\omega_p} = 3.34 \times 10^6 n_p^{-1/2},$$

where ω_p is the electron plasma frequency and n_p is the plasma density in cm^{-3} , can be optimized so as to maximize the energy gain of a sufficient number of particles to be detected by the imaging system. There is a tradeoff between maximizing the acceleration gradient and maximizing the number of particles that get accelerated. The electron bunch length has been measured to be 0.65 mm rms. Simulations (discussed in Sec. III) indicate that the plasma density is optimized when the plasma wavelength is equal to the total bunch ($4\sigma_z$), which gives $2.1 \times 10^{14} \text{e}^-/\text{cm}^{-3}$. For the plasma column length in this experiment of 1.4 m, operating at the transparency condition requires a density of $1.5 \times 10^{14} \text{e}^-/\text{cm}^{-3}$. Simulations performed for this lower plasma density indicate that reducing the plasma density has a minimal effect on the accelerating gradient and are discussed in Sec. III. The longitudinal density gradient in the plasma must be less than 15% to avoid a dephasing of more than $\pi/2$ with respect to the accelerating wake.

The neutral lithium vapor that is ionized to become the plasma must have two important characteristics. First, since the impact ionization cross section increases with atomic number Z , it must have a low atomic number to minimize the effect of impact ionization from the 30 GeV electrons. Second, it must have a low enough ionization potential to be ionized by an available laser system. Lithium (Li), with atomic number 3 and ionization potential of 5.392 eV makes a good choice.

A prototype for the photoionized Li plasma source has been described in detail elsewhere.¹⁵ A heat pipe oven provides a Li vapor column which is partially ionized by an excimer laser pulse. A stainless steel tube with an inner diameter of 30 mm is fitted with a wire mesh along its inner surface and wrapped on the outside with heater tapes to form

a heat pipe. The tube is filled with 30 g of solid Li and heated to $\sim 750^\circ\text{C}$. The heated Li becomes molten and Li vapor expands outwards toward cooling jackets at either end. These jackets are water cooled and work together with a helium (He) buffer gas to confine the Li vapor column and provide sharp (a few centimeters) Li/He longitudinal boundaries. The cooled Li vapor condenses, and is reheated while migrating back toward the oven center by wicking in the stainless steel wire mesh. The helium buffer gas is isolated from the beam line ultrahigh vacuum by 75- μm -thick beryllium windows.

An argon-fluorine (ArF) excimer laser provides 8 mJ of incident UV (193 nm, 6.45 eV photons) at the entrance to the Li vapor column. It has a rectangular cross section which is demagnified by a 3:1 telescope to an 8 mm^2 area at the entrance of the plasma, corresponding to a fluence of $\sim 100 \text{mJ}/\text{cm}^2$. The Li has an ionization potential of 5.392 eV and an ionization cross section of $1.8 \times 10^{-18} \text{cm}^2$ for the 6.45 eV photons.¹⁵ The UV telescope is adjusted to taper the spot size along the vapor column. This counteracts UV absorption by the Li vapor and maintains a constant fluence over the length of the plasma column.¹⁵ Longitudinal and transverse gradients in plasma density, resulting from damage to the optical elements, are being investigated. An approximately 10% ionization fraction ensures that the estimated 0.1% impact ionization of the Li vapor is negligible.

By measuring the incident and transmitted UV energy (E_i and E_t , respectively), and using the known ionization cross section of the neutral Li (σ), the line integrated number of neutral Li atoms along a column of length L can be calculated from the exponential attenuation of the photons through single photon ionization:

$$n_0 L = -\frac{1}{\sigma} \ln\left(\frac{E_t}{E_i}\right).$$

The UV energy at the Li-He boundaries can presently not be measured *in situ*. Thus, an additional measurement of UV transmission must be made when the oven is cold and no Li vapor is present. In this case any absorbed UV is due to losses in the air or optical elements such as windows, lenses, and pellicle mirrors. Further, the reflectivity and transmissivity of the various UV windows, lenses, and mirrors changes over time given the hostile environment in which they are operating—high incident laser energy density, x rays, and the electron beam itself. The optical elements degrade, typically over a few hours, and hence the plasma density calculated from UV absorption becomes more uncertain with integrated run time after the cold oven offset is measured. Mitigating damage to optical elements is an area of vigorous activity in the ongoing experiment.

For the purpose of developing an independent diagnostic for the neutral and plasma density, systematic studies of Cherenkov radiation immediately downstream from the oven at wavelengths near the spectral line of Li neutrals (670 nm) have been performed. Measurement of the Cherenkov cone angle permits direct estimate of the neutral density seen by the electron beam, since the Cherenkov resonance condition depends directly on this quantity.¹⁶

C. Optical transition radiation diagnostics

The pellicle mirrors that couple the ionization laser pulse into the plasma (see Fig. 1) are 150- μm -thick fused silica substrates with a multilayer dielectric high reflectivity (HR) coating for 193 nm. By depositing a thin film of aluminum onto the side opposite the HR coating they serve an additional role as sources of OTR at close proximity to the plasma entrance and exit. OTR provides a convenient, non-destructive way to measure the beam transverse profile on a single pulse basis. The electron beam undergoes betatron oscillations as it travels down the length of the plasma. In principle, OTR images downstream of the plasma allow for tuning the plasma density such that the beam envelope undergoes an integer number of oscillations and the plasma can be considered transparent to the transverse dynamics. In practice, fluctuations in laser energy give rise to fluctuations in the plasma density and the downstream OTR serves to monitor these deviations from the ideal.

The validity of OTR as a diagnostic for multi-GeV beams was recently confirmed as part of an E-157 test run at SLAC¹⁷ in which 50 μm spot sizes were resolved, in agreement with independent measurements. Although the radiation peaks at an angle $1/\gamma$, at multi-GeV energies a large fraction of the radiation is in the wings of the distribution and has consequences for the resolution of an OTR-based imaging system. The full width half-maximum (FWHM) of an image of a point source, resolved using OTR, is obtained by integrating the single point function, but can be estimated for an optical system of angular acceptance (θ_a) and wavelength λ :¹⁸

$$\text{FWHM} \cong \frac{1.44\lambda}{\theta_a}.$$

OTR from the aluminum coating exits the vacuum through a viewport and is imaged onto a charge-coupled device (CCD) camera by a high-resolution compound lens. The angular acceptance is sufficient for a total resolution of the order of 10 μm . The overall resolution, which includes effects from finite pixel size, etc., is typically larger, on the order of 20 μm . Images from the cooled CCD cameras, with dynamic ranges of 12 and 16 bits, are digitized by computers that tag the images and store them to disk.

D. Cherenkov radiation diagnostic

As discussed in Sec. III, the peak accelerating field occurs in the back of the electron bunch. As the accelerating gradient increases within the electron bunch, the number of electrons present to witness the accelerating field is progressively lower. Additionally, the number of accelerated electrons that can be resolved is directly proportional to the number of photons created and transported to the streak camera. Recent measurements at SLAC demonstrated that an aerogel-based Cherenkov system delivered a factor of 20 more photons than an OTR-based system for similar beam conditions.¹⁹ Measuring the combined effects of the transverse and longitudinal fields as depicted in Figs. 2–5, requires measuring the beam energy as a function of time with spatial resolutions of the order of 150 μm (corresponding to

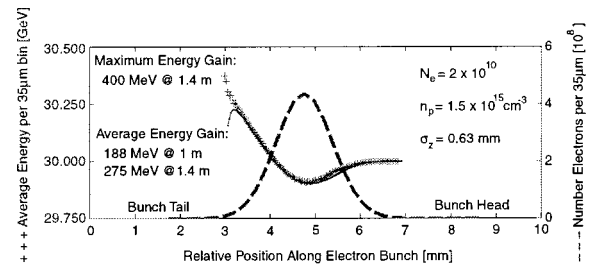


FIG. 2. Simulation results predicting the core of the electron bunch should lose up to 125 MeV creating the plasma wake, while particles in the tail should gain an average energy of 275 MeV with a maximum energy of 400 MeV.

an energy resolution of 50 MeV) and a temporal resolution of 1 ps, respectively. Since housing the streak camera in the radiation enclosure of the FFTB beamline is undesirable due to the limited access afforded, the aerogel radiator is imaged onto the slit of the streak camera located outside the radiation shielding some 15 m away. All reflective optics are used to prevent temporal resolution degradation due to dispersion in transmissive optical elements. The mirrors are coated with an enhanced aluminum coating that is 90%–95% reflective

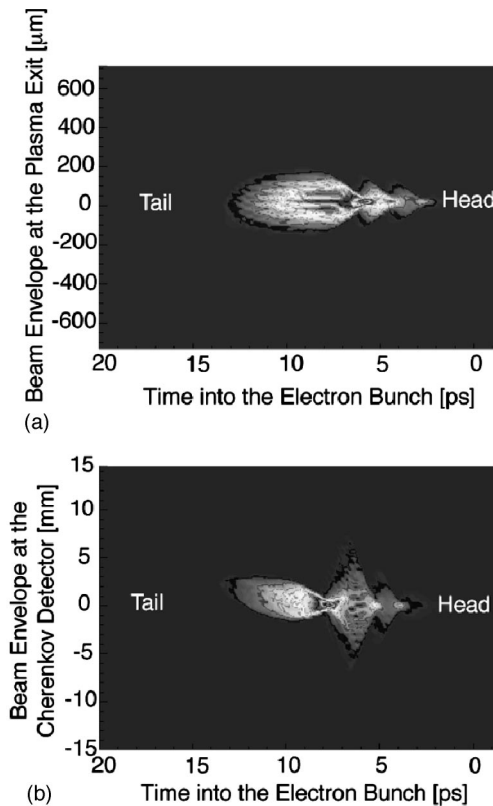


FIG. 3. Simulations showing an electron bunch of 2×10^{10} electrons, with an initial tilt of 10 μm radially per σ_z , at the exit of the plasma. The bunch undergoes a total of three envelope oscillations within the 1.4 m plasma column of density $1.5 \times 10^{14} \text{ e}^-/\text{cm}^3$. (a) The bunch at the exit of the plasma. (b) The same bunch propagated 12 m downstream to the Cherenkov detector (not including energy dispersion). With an initial tilt on the bunch, the tail could exit the plasma with enough divergence to cause offsets on the order of a few millimeters when propagated 12 m downstream to the Cherenkov detector.

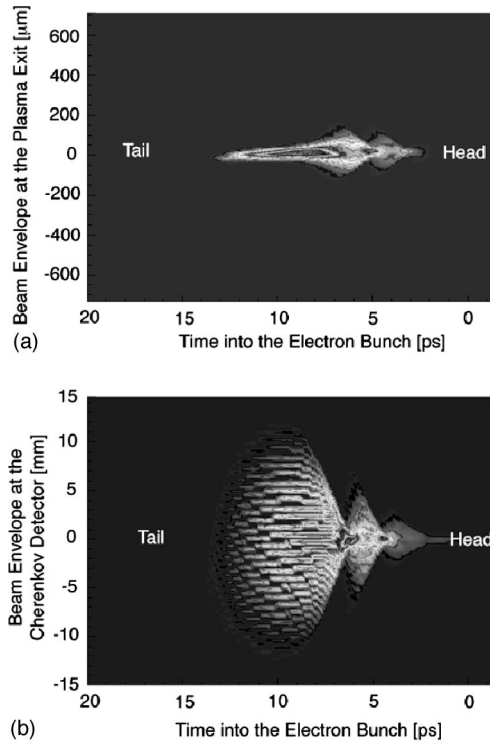


FIG. 4. Simulations showing an electron bunch of 2×10^{10} electrons exiting the plasma after undergoing only 2.5 envelope oscillations within the plasma. (a) The bunch at the exit of the plasma, (b) the same bunch propagated 12 m downstream to the Cherenkov detector (not including dispersion). The beam exits the plasma at a waist with a large divergence that results in the beam blowing up to such an extent that the transverse size and divergence would obscure the energy measurements.

over the bulk of the visible spectrum (400–700 nm), resulting in an overall transmission efficiency of roughly 25%. Field mirrors allow for a field of view (FOV) of ~ 7 mm. For an electron beam energy of 30 GeV and a dispersion (η) of 0.085 m, this corresponds to a total imaged energy spread of up to

$$\Delta E = E \frac{\text{FOV}}{\eta} = 2.5 \text{ GeV}.$$

Spatial resolution is of the order of $100 \mu\text{m}$ and temporal resolution (including the contribution from the streak camera entrance slit width) is 1 ps. A beam splitter samples a fraction of the Cherenkov light and provides a time-integrated image of the beam in the transverse plane. Monitoring the transverse size provides an additional diagnostic as well as ensuring that alignment of the electron beam image onto the slit is maintained for both the plasma on and plasma off conditions.

III. SIMULATIONS AND PREDICTIONS

Fully self-consistent particle-in-cell simulations have been performed in two and three dimensions using the object-oriented parallel code OSIRIS.²⁰ The code employs a moving window to follow the beam and was run on up to 64 nodes on the Cray T3E at the National Energy Research

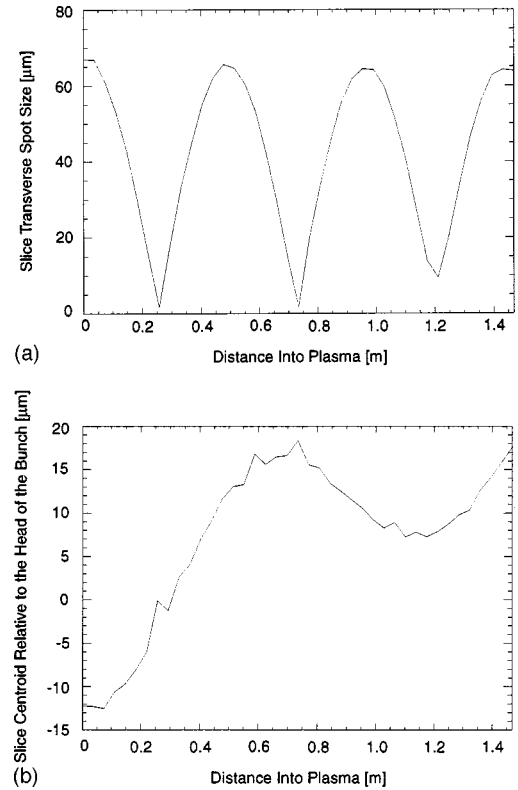


FIG. 5. Simulations showing the effect of the plasma on a beam that enters the plasma with a vertical tilt of $10 \mu\text{m}$ per σ_z . Although the envelope of this particular tail slice ($440 \mu\text{m}$ back from the head) may undergo three oscillations (a), the centroid oscillates about the head of the beam at slightly less than half the envelope frequency (b). Particles in the tail can thus exit the plasma with up to $320 \mu\text{rad}$ of divergence, which leads to offsets of the order of a few millimeters when propagated 12 m downstream to the Cherenkov detector.

Scientific Computing Center (NERSC). Simulation results for the energy gain, beam profiles, and betatron behavior are shown in Figs. 2–5.

Figure 2 shows the energy gain of the beam in a plasma of density $1.5 \times 10^{14} \text{ cm}^{-3}$ in a 2-D simulation with axisymmetric cylindrical geometry. Also shown are the number of particles and the maximum particle energy in 0.122 ps bins along the z axis. For this case, the bunch contained 2×10^{10} electrons in a bi-Gaussian round bunch of length $\sigma_z = 0.63 \text{ mm}$, transverse spot size $\sigma_r = 70 \mu\text{m}$, and emittance of 15 mm mrad . The maximum energy bin had a bin-averaged energy gain of 250 MeV and the highest energy particle gained 400 MeV. It should be noted that the accelerating gradient scales with the electron bunch charge and inversely with the electron bunch length squared. Future efforts will study the effects of increasing the electron bunch charge by up to a factor of 2 and/or decreasing the electron bunch length by 30%.

Figures 3 and 4 show images from three-dimensional (3-D) simulations of the beam (y vs z) at the exit of the plasma and again after 12 m of free space propagation to the Cherenkov detector (not including energy dispersion from the magnet). In order to simulate head–tail offsets of the type that can occur in the experiment, the beam was initialized with a linear cant in the y direction of $10 \mu\text{m}$ per σ_z (0.63

mm). In Fig. 3 the beam is exiting the plasma at $z = 1.4$ m after three envelope oscillations (see Fig. 5), while in Fig. 4 it exits after 2.5 envelope oscillations. In the experiment, the spot size measured at the Cherenkov detector is a combination of both the transverse size and the dispersed energy spectrum of the electron beam, adding together in quadrature. The blowup of the beam in Fig. 4(b) illustrates how in the experiment a beam diverging at the plasma exit can dominate the measured beam spot size when compared to the contribution from the energy spectrum. Operating at plasma conditions corresponding to an integer number of envelope oscillations minimizes the beam divergence and the subsequent contribution to the time-resolved energy measurement.

Figure 5 shows the y centroid and y -spot size of an axial slice $440 \mu\text{m}$ behind the center of the beam as a function of distance propagated into the plasma (corresponding to the 3-D simulation of Fig. 3). We see the regular oscillations of the spot size. The centroid of this slice is initially at $y = -7 \mu\text{m}$ and oscillates approximately about an axis defined by the head of the beam at $y = +7 \mu\text{m}$. The period of the tail flipping apparent in Fig. 5(b) is roughly twice the period of the envelope oscillations. Therefore, if the electron beam enters the plasma with a head-to-tail offset or tilt, the tail of the beam will oscillate due to the perpendicular wake fields and could even grow due to the hosing instability.^{12,20} The 3-D simulations shown in Fig. 5(b) indicate that although the plasma density may be such that the bulk of the beam exits the plasma with a phase advance of 3π , the tail is slightly out of phase with the bulk of the beam. Consequently, the tail of the beam can exit the plasma with a significant divergence ($160\text{--}320 \mu\text{rad}$), which when propagated 12 m downstream to the Cherenkov detector, can lead to tail offsets of several millimeters [see Fig. 3(b)]. Such an offset is of the same order, and convoluted with, offsets due to changes in electron energy (see Sec. III D).

IV. EXPERIMENTAL DATA

As mentioned in Sec. I, there are several distinct experimental observables in addition to the acceleration of electrons in the tail of the drive bunch. First, for a given length of plasma, the electron beam undergoes betatron oscillations once the ion channel is established. These produce plasma-density-dependent oscillations of the spot size of the electron beam downstream of the plasma. The transverse focusing forces of the ion column should result in betatron oscillations within the plasma of betatron wavelength (λ_β)

$$\lambda_\beta = \sqrt{2} \gamma \lambda_p,$$

where γ is the relativistic factor. Figure 6 shows the beam undergoing the first envelope oscillation on the time-integrated Cherenkov detector. The plasma density is varied by changing the relative delay between the ionization laser pulse and the arrival of the electron beam, allowing the plasma to decay due to recombination and diffusion. Ideally, the experiment is conducted at a plasma density corresponding to an integer number of beam envelope oscillations to minimize the contribution of transverse dynamics to the time-resolved energy measurement. In practice, fluctuations

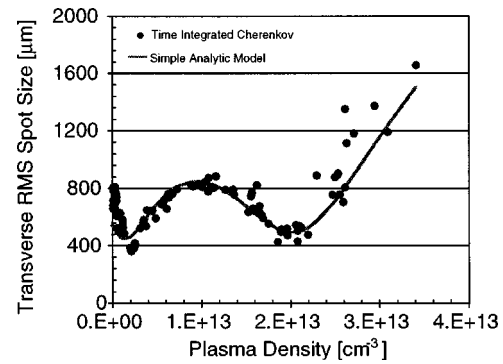


FIG. 6. The time-integrated transverse spot size of the electron beam measured at the Cherenkov detector. As the plasma density (estimated from the UV absorption measurement) is increased to a few $10^{13} \text{ e}^-/\text{cm}^3$, the beam gradually focuses, blows up, and then refocuses at the detector as the beam undergoes the first envelope oscillation.

in both the ionization laser energy (plasma density) and the incoming electron beam distribution necessitate reducing the data based on information such as the laser energy and beam size downstream of the plasma.

Second, during the rise time of the electron bunch, while the ion channel is being formed, different parts of the beam will undergo a different number of envelope oscillations. This will manifest itself as time-dependent defocusing and focusing along the electron bunch. For the simulations shown in Figs. 3(a) and 3(b), the three envelope oscillations are visible in the head of the bunch. The 1 ps resolution of the streak camera diagnostic only resolves the envelope of these oscillations at the head of the bunch.

Due to variations in electron beam tails and ionization laser pulse energy, the diagnostics show a wide variety of images. Figure 7(b) shows a time-resolved image of the electron beam at the Cherenkov detector, selected because it illustrates many of the effects predicted by the simulations. Figure 7(a) is a case with plasma off and Fig. 7(b) is with the plasma turned on. In Fig. 8, the images from Fig. 7 have been processed to illustrate the time-dependent features. The images in Fig. 7 have been divided into 1.3 ps slices. Each slice is then projected onto the vertical axis and fit to a Gaussian. The central contours show the centroid and rms widths of the individual slices. When the projections are non-Gaussian, however, the fits do not take into account particles out in the wings. The additional contours in Fig. 8 show the maximum extent of particles registering intensities of 50% and 30% of the maximum, respectively.

In the plasma off case the beam is roughly cylindrical with no longitudinal correlation in beam energy. Once the plasma is turned on, however, the time-resolved image in Fig. 7(b), as well as the contours in Fig. 8(b) show many of the qualitative features predicted by the simulations. The head of the beam defocuses to ~ 1.5 times the initial transverse size as the electrons are being blown-out, then pinches back down to nearly its initial size after the ion channel is formed. Third, in the back of the beam where the accelerating gradient is large, there is a shift of particles in the direction of increasing energy.

To differentiate the effect of the transverse dynamics

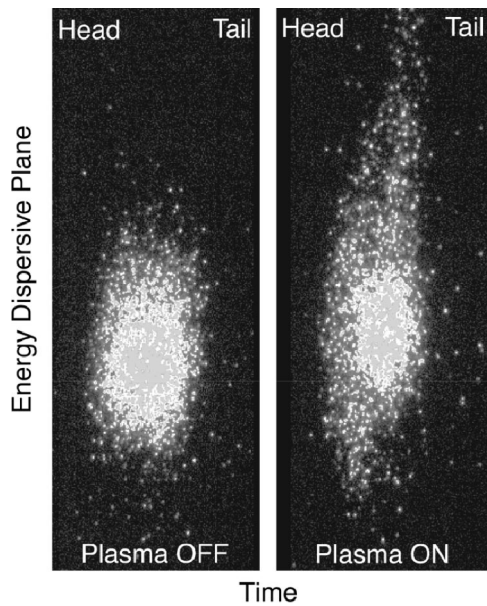


FIG. 7. Selected time-resolved images of the electron beam size in the energy dispersive plane for plasma off (a) and plasma on (b).

(deflections of tails) from the longitudinal dynamics (acceleration of tails), two techniques are typically employed. First, “bumps” are placed into the electron beam orbit upstream of the plasma to manipulate the transverse wake fields and deliberately introduce tails into the beam such that their deflection by the plasma can be studied. Second, the plasma density is changed from the nominal operating density, which corresponds to three envelope oscillations, to a lower density corresponding to two envelope oscillations. After two oscillations in the plasma, an electron emerges with the same radial position and angle as it enters. After three oscillations, an electron exits the plasma with a radial position and momentum opposite to how it entered. This results in “tail flipping.” These two techniques are used to understand and minimize the contributions to the energy measurement resulting from transverse kicks. When analyzing candidate images for acceleration, these effects have to be considered and quantified—improving our understanding of tail effects is ongoing.

The head of the bunch deposits energy into plasma wakes, resulting in a longitudinal accelerating field which is then witnessed by the tail of the same bunch. For a beam of 2×10^{10} electrons and a plasma density of 1.5×10^{14} , Fig. 2 predicts that the core of the beam should deaccelerate by up to 100 MeV as it creates the plasma wake. An energy loss of 100 MeV corresponds to a change in the centroid location by $-285 \mu\text{m}$ at the Cherenkov detector. In the tail of the bunch, where particles witness the longitudinal wake, electrons gain energies up to 400 MeV, corresponding to an upward shift of 1.2 mm. Quantifying the exact values for energy gain and loss via improved statistics and understanding the contributions from transverse effects is the focus of this ongoing experiment.

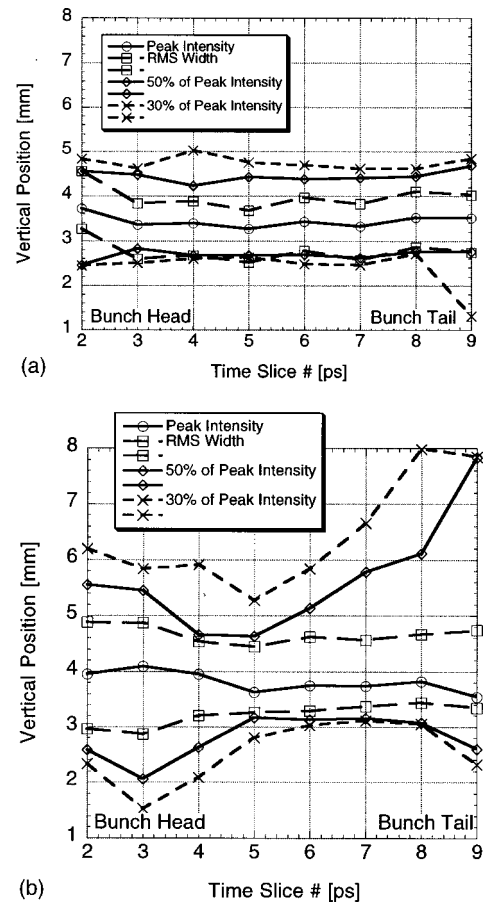


FIG. 8. The Figures 7(a) and 7(b) are divided into slices 1.3 ps wide, projected onto the vertical (energy dispersive) axis, and then fitted to Gaussians. The position of the peak value as well as the rms width of the individual slices is plotted versus slice number for both plasma off (a) and plasma on (b). Additional contours showing the farthest extent of counts having an amplitude of 50% and 30% of the peak value of each individual slice are also plotted.

V. CONCLUSIONS

In the ongoing plasma wake field acceleration experiment E-157, several characteristics of the transverse and longitudinal dynamics predicted by simulations have been observed. The beam transverse size is not matched to the focusing channel produced by the blow-out of the plasma electrons. This results in a modulation of the transverse size of the electron beam downstream of the plasma as a function of the plasma density. Within the rise time of the electron beam, while the ion channel is being formed, different parts of the beam undergo a different number of envelope oscillations, and are manifested as time-dependent defocusing and focusing of the front of the beam. Quantifying the energy loss of the core and energy gain of the tail, through an improved understanding of the contributions from the deflection of wake field tails, is the focus of ongoing efforts.

ACKNOWLEDGMENTS

The authors wish to thank Dr. Peter Tsou of the Jet Propulsion Laboratory for providing the aerogel for the Cherenkov detector. Work supported by Department of Energy Contract Nos. DE-AC03-76SF00515, DE-AC-03-

76SF0098, and DE-FG03-98-DP-00211, National Science Foundation Contract Nos. ECS9617089 and DMS-9722171, and Lawrence Livermore National Laboratory Contract No. WO7405-ENG-48.

Color versions of figures available upon request.²¹

- ¹E. Esarey, P. Sprangle, J. Krall *et al.*, IEEE Trans. Plasma Sci. **24**, 252 (1996).
- ²T. Tajima and J. M. Dawson, Phys. Rev. Lett. **43**, 267 (1979); M. N. Rosenbluth and C. S. Liu, *ibid.* **29**, 710 (1972).
- ³P. Chen, J. M. Dawson, R. W. Huff *et al.*, Phys. Rev. Lett. **54**, 693 (1985); R. D. Ruth, A. W. Chao, P. L. Morton *et al.*, Part. Accel. **17**, 171 (1985).
- ⁴C. E. Clayton, K. A. Marsh, A. Dawson *et al.*, Phys. Rev. Lett. **70**, 37 (1993); J. B. Rosenzweig, D. B. Cline, B. Cole *et al.*, *ibid.* **61**, 98 (1998); F. Amiranoff, D. Bernard, B. Cros *et al.*, Phys. Rev. Lett. **74**, 5220 (1995).
- ⁵M. Everett, A. Lal, D. Gordon *et al.*, Nature (London) **368**, 527 (1994).
- ⁶F. Amiranoff, S. Baton, D. Bernard *et al.*, Phys. Rev. Lett. **81**, 995 (1998).
- ⁷A. Modena, Z. Najmudin, A. E. Dangor *et al.*, Nature (London) **337**, 606 (1995); K. Nakajima, D. Fisher, T. Kawakubo *et al.*, Phys. Rev. Lett. **74**, 4428 (1995); C. I. Moore, A. Ting, K. Krushelnick *et al.*, *ibid.* **79**, 3909 (1997); R. Wagner, S.-Y. Chen, A. Maksimchuk *et al.*, *ibid.* **78**, 3125 (1997).
- ⁸D. Gordon, K. C. Tzeng, C. E. Clayton *et al.*, Phys. Rev. Lett. **80**, 2133 (1998).
- ⁹J. B. Rosenzweig, D. B. Cline, B. Cole *et al.*, Phys. Rev. Lett. **61**, 98 (1998).
- ¹⁰R. Assmann, P. Chen, F. J. Decker *et al.*, Nucl. Instrum. Methods Phys. Res. A **410**, 396 (1998).
- ¹¹J. B. Rosenzweig, B. Breizman, T. Katsouleas *et al.*, Phys. Rev. A **44**, 6189 (1991); N. Barov, J. B. Rosenzweig, M. E. Conde *et al.*, Phys. Rev. ST-AB **3**, 011301 (2000).
- ¹²M. Lampe, G. Joyce, S. P. Slinker *et al.*, Phys. Fluids B **5**, 1888 (1993); J. Krall and G. Joyce, Phys. Plasmas **2**, 1326 (1995); D. H. Whittum, Phys. Fluids B **5**, 12 (1993).
- ¹³J. T. Seeman, *Proceedings of the 1999 Particle Accelerator Conference* (IEEE, Piscataway, NJ, 1999).
- ¹⁴V. E. Balakin, A. V. Novokhatsky, and V. P. Smirnov, Proceedings of the 12th International Conference on High Energy Accelerators, Batavia, IL, 1983 (unpublished).
- ¹⁵P. Muggli *et al.*, *Proceedings of the Third Annual ICFA Conference on Second Generation Plasma Based Accelerators*, in *IEEE Transactions on Plasma Science*, 1999; S. DiMaggio, L. Archambault, P. Catravas *et al.*, in Ref. 13.
- ¹⁶P. Catravas (private communication).
- ¹⁷P. Catravas, W. P. Leemans, E. Esarey *et al.*, in Ref. 13.
- ¹⁸V. A. Lebedev, Nucl. Instrum. Methods Phys. Res. A **372**, 344 (1996); M. Castellano and V. A. Verzilov, Phys. Rev. ST Accel. Beams **1**, 062801 (1998).
- ¹⁹R. Assmann, P. Chen, F.-J. Decker *et al.*, in Ref. 13.
- ²⁰R. G. Hemker, F. S. Tsung, V. K. Decyk *et al.*, in Ref. 13.
- ²¹See AIP Document No. E-PAPSE-PHPAEN-7-978005 for color versions of figures. E-PAPS document files may be retrieved free of charge from our FTP server (<http://www.aip.org/pubservs/epaps.html>) or from [ftp.aip.org](ftp://ftp.aip.org) in the directory /epaps/. For further information, e-mail: paps@aip.org or fax: 631-576-2223.

Appendix III

Collective Refraction of a Beam of Electrons at a Plasma-Gas Interface

Patrick Muggli, Seung Lee, Thomas Katsouleas, Ralph Assmann, Franz-Josef Decker, Mark Hogan, Ralph Iverson, Pantaleo Raimondi, Robert Siemann, Dieter Walz, Brent Blue, Chris Clayton, Evan Dodd, Ricardo A. Fonseca, Ray Hemker, Chan Joshi, Ken Marsh, Warren B. Mori, Shoquin Wang
Submitted to *Nature*

Collective Refraction of a Beam of Electrons at a Plasma-Gas Interface

Patrick Muggli*, Seung Lee*, Thomas Katsouleas*, Ralph Assmann‡, Franz.-Josef Decker†, Mark Hogan†, Ralph Iverson†, Pantaleo Raimondi†, Robert Siemann†, Dieter Walz†, Brent Blue§, Chris Clayton§, Evan Dodd§, Ricardo A. Fonseca§//, Ray Hemker§, Chan Joshi§, Ken Marsh§, Warren B. Mori§ & Shoquin Wang§

**University of Southern California, Los Angeles, California 90089, USA*

†Stanford Linear Accelerator Center, Stanford University, Stanford, California 94309, USA

§University of California Los Angeles, Los Angeles, California 90095, USA

‡Present address : CERN, Geneva, Switzerland

// Visiting from GoLP/Centro de Fisica dos Plasmas Instituto Superior Tecnico, 1049-001, Lisboa, Portugal

The refraction of light at an interface is as familiar as rainbows and “bent” pencils in a glass of water. The refraction of charged particles at an interface between two media on the other hand is not commonly considered. Take for example the case of a 30 GeV electron incident on water. The refraction takes the form of a small amount of random scattering^{1,2} – an rms scattering angle of 20 micro-radians after one millimeter. In this letter we report the collective refraction of a 30 GeV beam of electrons at a plasma/gas interface that is orders of magnitude larger than would be expected from single electron considerations and that is unidirectional. Although the density of nuclei is ten million times less than that of the water example above, the collective response of the plasma produces a deflection of the electron beam of the order of one milliradian. The electron beam exiting the plasma is bent away from the normal to the interface in analogy with light exiting from a higher index medium.

To understand the physical picture of this collective refraction mechanism, consider the geometry shown in Fig. 1. A dense beam of electrons is incident from the plasma side on a planar boundary between a medium of ionized plasma gas and un-ionized gas. For simplicity we neglect the small effect of Coulomb scattering by the gas and treat the boundary as between plasma and vacuum. We consider the case of dense beams or underdense plasmas such that the beam’s density n_b is greater than the plasma density n_0 . While the beam is fully in the plasma, the space charge at the head of the beam repels the plasma electrons out to a radius r_c ³. The remaining plasma ions constitute a positive charge channel through which the latter part of the

beam travels. The ions provide a net focusing force on the beam ⁴. When the beam nears the plasma boundary, the ion channel becomes asymmetric producing a deflecting force in addition to the focusing force. This asymmetric plasma lensing gives rise to the bending of the beam path at the interface. The bending of the beam by the collective effect of the (passive) medium at the boundary is the particle analog to refraction of photons at a dielectric boundary ⁵.

To estimate the order of magnitude of this deflection, consider the simple case of the beam at the edge of a sharp plasma boundary (Fig. 1b) of density n_o . The beam of radius r_b and density n_b has a positive ion charge column on one side of radius $r_c = (n_b/n_o)^{1/2} r_b$, where γ is 1 for long beams ³ and approximately 2 for beams of length on the order of the plasma wavelength ⁶ (due to a resonant overshoot of the expelled electrons). For beams shorter than the plasma wavelength (λ_p) there is not enough time for the channel to reach its full extent and r_c can be shown to scale as $\frac{4}{c} \frac{z}{\lambda_p}$, where z is the Gaussian bunch length and c/λ_p is the plasma skin depth ($\lambda_p/2 = c/\sqrt{4 n_o e^2 / m}$). At the edge of the column is a layer of electrons with a total charge equal and opposite to that in the ion column; and on the other side of the beam there is no charge ⁷. The nearby positive charge will attract the beam toward the center of the plasma. The electric field at the beam is easily estimated for this picture from Coulomb's law applied to a cylinder with the cross-section shown in Fig. 1b, yielding

$$F = -eE = 2n_o e^2 r_c \quad (1)$$

The impulse on the beam is found by multiplying this force by the time that the beam is within a channel radius of the edge. The time spent near the edges is $2r_c/c \sin \theta$, where θ is the angle between the beam and plasma boundary. Dividing by the particles' parallel momentum γmc gives a scaling law for the deflection angle θ valid for θ greater than $\pi/4$:

$$\theta = \frac{8}{\sqrt{2}} \frac{N r_e}{z \sin \theta} \quad (2)$$

where $N/\sqrt{2} z$ is the charge per unit length of the beam and r_e is the classical electron radius. Note that for long beams compared to the plasma skin depth (or equivalently, high plasma densities) such that θ is constant, the dependence of θ on plasma density cancels out. This is

because higher density, although giving a stronger deflection force, gives a narrower channel and hence a shorter time for the impulse.

We note that the impulse approximation used in obtaining Eq. (2) breaks down at small incident angles such that the deflection is on the order of λ . In this case, the beam can be internally reflected. From the simulations, when θ is less than θ_c above, the beam is deflected just enough to skim along the interface. That is

$$\theta \sim \theta_c \quad (3)$$

for small angles θ .

The simple analytic model above was tested with the electron beam from the Stanford Linear Accelerator Center (SLAC) linac at the Final Focus Test Facility. The experimental setup has been described in Ref. 9. The plasma was created by photoionization of a column of lithium vapor by an ArF laser (193nm, 14 mJ, 5 ns). The plasma density was $1-2 \times 10^{14} \text{ cm}^{-3}$ with a cross section of approximately $2.5 \text{ mm} \times 2.1 \text{ mm}$ and length of 1.4 m. The beam consisted of 1.9×10^{10} electrons at 28.5 GeV in a Gaussian bunch of length $\sigma_z = 0.7 \text{ mm}$ and spot size $\sigma_x \sim \sigma_y \sim 40 \text{ }\mu\text{m}$. The electron beam traversed a thin glass pellicle located 57 cm before the plasma, and overlapped with the ionizing laser beam that reflected off the same pellicle. The angle between the electron bunch initial trajectory and the laser beam (in Eq. 2) was remotely adjusted using the pellicle tip-tilt angle, and was monitored by measuring the deflection of a reference HeNe laser. The electron beam propagated over a distance of about 12 m after the plasma and its shape and transverse position at that location were measured using a Cerenkov radiator (1mm long aerogel) and an imaging system. The transverse position was also monitored independently at several other locations downstream of the plasma, including a beam position monitor 4.3m downstream. Sample results are shown in Figs. 2 and 3.

To compare to the experiments as well as to provide further insight into the physical mechanisms involved in the refraction we performed fully self-consistent, electromagnetic particle-in-cell simulations in three dimensions¹⁰. Fig. 2c shows a snapshot of the real space of the beam and plasma electron density (blue) from a simulation. The head of the beam has emerged undeflected from the plasma at this time, but the tail portion has been deflected toward

the plasma and is near the plasma boundary. This results in a characteristic splitting of the beam downstream into two as seen in Figs. 2b and 2d.

The apparent break-up of the beam into bunchlets can be understood in the following way. There is a focusing force from the plasma that increases from head to tail as the plasma responds to the beam ⁶. The head is not focused, but as the plasma responds, the ion column forms producing focusing, and the first waist that forms has separated the head from the next bunchlet. This bunchlet is separated from the remainder of the beam by another waist. Note that once plasma blowout occurs, the remainder of the beam has the same focusing and deflection angle.

Figure 3 is a plot of beam deflection () measured with the beam position monitor versus angle between the laser and the beam (). The solid curve is the prediction from the impulse model. For incident angles less than 1.3 mrad, the beam appears to be internally reflected in agreement with Eqs. (2) and (3).

The simulations and experimental results presented here show that it is possible to refract or even reflect a particle beam from a dilute plasma gas. Remarkably, for a 28.5 GeV beam, the collective effects of a plasma are strong enough to "bounce" the beam off of an interface one million times less dense than air. It is possible to ascribe to the plasma an effective index of refraction and corresponding Snell's law for this collective phenomenon. However, the refractive index is angle-dependent and intrinsically nonlinear, and we leave it for a future paper.

The refraction and total internal reflection of light obviously have many significant applications such as the guiding of light pulses in optical fibers. It is interesting to contemplate the possibility of a similar use of internal reflection of particles to guide electricity in "vapor wires" that are rapidly created or reconfigured by shining laser beams through a gas. One can imagine fast optical kickers replacing magnetic kickers or even compact magnetless storage rings. For such applications it will probably be necessary to use an auxiliary laser or particle beam (which may be of much lower energy) to pre-form the ion channel and deflect all of a trailing particle beam. As an example, consider a gas that is ionized to a density of 10^{16} cm^{-3} by a laser that propagates at an angle of a few milliradians to the path of a focused electron beam. For beam parameters typical of SLAC, the deflection force (Eq. 2) is equivalent to a 50 kG dipole magnet, and the turn-on time is approximately $\tau_p^{-1} = 200$ femtoseconds.

References

1. *Stars As Laboratories for Fundamental Physics*, p. 199, Raffelt, U. G. Chicago Press (Chicago, 1996).
2. *Theoretical Physics*, 2nd ed., p. 687, Joos, G., Hafner, G. (New York, 1959).
3. Whittum, D., Sessler, A. and Dawson, J., “Ion-Channel Laser,” *Phys. Rev. Lett.* **64**, 2511 (1990).
4. Su, J.J., T. Katsouleas, T. and Dawson, J.M. *Phys. Rev. A* **41**, 3321 (1990); Chen, P., *Part. Accel.* **20**, 171 (1987).
5. The refraction of the particle beam considered here is quite different from other more familiar bending mechanisms for particle beams: for example, the bending of a beam by a magnetic field. Unlike the magnetic case, the bending here is a boundary effect. It is caused by a field free (initially) passive medium, and in this sense is analogous to optical refraction at a dielectric boundary.
6. Lee, S., Katsouleas, T., Hemker, R., Mori, W.B., “Simulations of a meter long plasma wakefield accelerator,” *Phys. Rev. E* **61**, 7014 (2000); Lampe, M., et al., *Phys. Fluids B* **5**, 1888 (1993); Barov, N., et al., *Phys. Rev. Lett.* **80**, 81 (1998); Hemker, R., Mori, W.B., Lee, S., Katsouleas, T., “Dynamic effects in plasma wakefield excitation,” *Phys. Rev. Special Topics-AB* **3** (6) (2000).
7. When the beam center is near the boundary but still inside the plasma, some plasma electrons (the ones above the beam axis) are expelled from the plasma. These electrons are attracted back to the ion column after the passage of the beam. Once the beam center crosses the boundary, all plasma electrons ahead of the beam will be blown inward, and the simple physical description in the text applies.
8. The fields surrounding an axial slice of a relativistic beam depend only on the currents and charge in the same slice. This follows from developing the wave equation from Ampere’s and Faraday’s laws and noting that for wake-like solutions and beams at speed near c , $d/dz - 1/c d/dt = 0$. Thus the fields at a slice can be found by assuming the slice to be an infinite cylinder. Whittum, D. “Transverse two-stream instability of a beam with a Bennett profile,” *Phys. Plasmas* **4**, 1154 (1997).
9. Hogan, M.J., et al., “E-157: A 1.4 meter-long plasma wakefield experiment using a 30 GeV electron beam from the Stanford Linear Accelerator Center Linac,” *Phys. Plasmas* **7**, 224 (2000).
10. Hemker, R., et al., *Proc. PAC 99*, p. 3672, IEEE Catalog No. CH36366 (1999).

Acknowledgements

We would like to acknowledge the godfather of this collaboration, John M. Dawson. We thank Luis O. Silva for useful discussions and our collaborators on prior work leading to this experiment: W.P. Leemans, P. Catravas, E. Esarey, S. Chattopadhyay, P. Volfbeyn, and D. Whittum; as well as S. Rokni and T. Kosteroglou. We thank Phil Muntz of USC for generously sharing his laser and Dr. Peter Tsou of JPL for providing the aerogel.

Correspondence and requests for materials should be addressed to T.C.K.
(email: katsoule@usc.edu).

Figure Captions

Figure 1. Schematic of refraction mechanism: a) side view and b) front view of beam and plasma illustrating how asymmetric blowout creates a net deflection force.

Figure 2. Images of the electron beam showing refraction of a portion of the beam: a) Cerenkov image without the plasma (i.e., laser off). b) Cerenkov image with the laser on at an angle of 1 mrad to the beam. Cross-hairs show the undeflected beam location. c) PIC simulation of electron beam, side view with plasma shown (blue). The inward motion of the plasma electrons is visible as a depression in the blue plasma surface behind the beam. d) PIC simulation, head on view corresponding to (b). The code used was OSIRIS and is described in Ref. 10. Simulation parameters: beam energy of 30 GeV, beam charge of 3.2 nCoul in a bi-Gaussian distribution (spot size $r_r=70\mu\text{m}$, bunch length $z=0.63\text{ mm}$) incident on a plasma of density $2 \times 10^{14}\text{ cm}^{-3}$. In the simulation, the beam propagated through approximately 80 cm of plasma before encountering a sharp plasma/vacuum boundary at an incident angle of 0.9 mrad in the x-z plane. The model consisted of 2×10^7 particles on a $160 \times 120 \times 88$ grid representing a $2.9\text{mm} \times 2.2\text{mm} \times 6.5\text{mm}$ section of plasma (x,y,z) moving with the beam (z-direction).

Figure 3. Experimentally measured electron beam deflection as a function of angle between laser and e-beam (i.e., angle of incidence θ). Solid curve is the impulse model from Eqs. (2) and (3) with $\beta=1.4$ for the bunch length and plasma density corresponding to this run (0.7 mm and $1 \times 10^{14}\text{ cm}^{-3}$, respectively). Since the beam deflection measured by the beam position monitor is a weighted average over the entire beam, it is less than one would obtain for the peak deflection of the tail portion of the beam. To compare to the data, the impulse model has been scaled by an overall factor (0.17). Note that the critical angle for total internal reflection (the cusp in the figure) is independent of the choice of scaling factor.

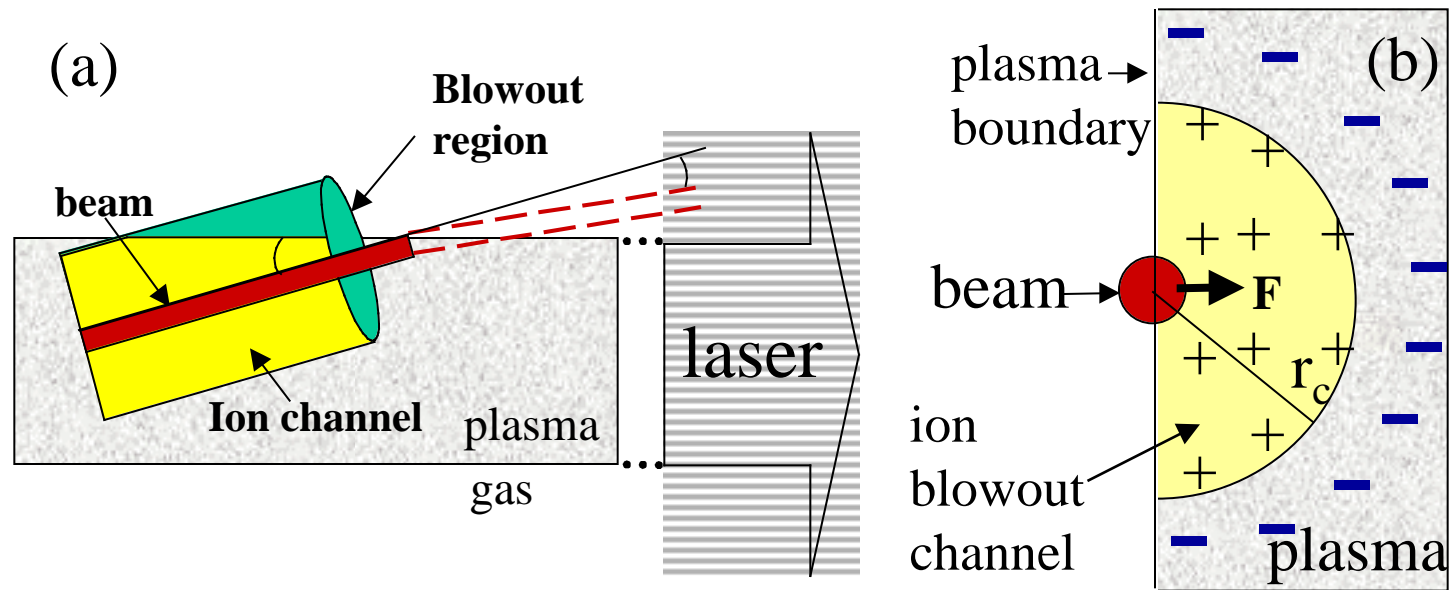
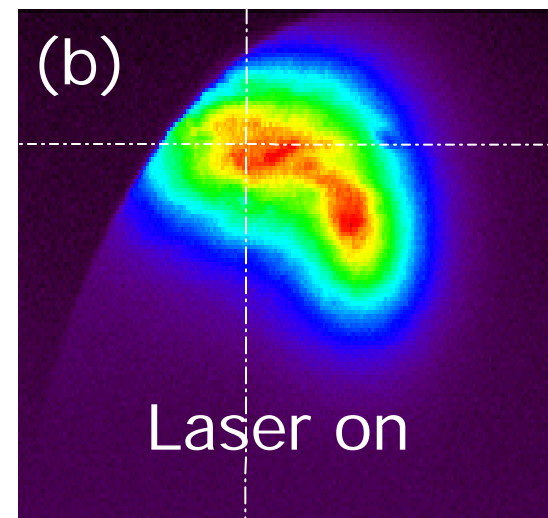
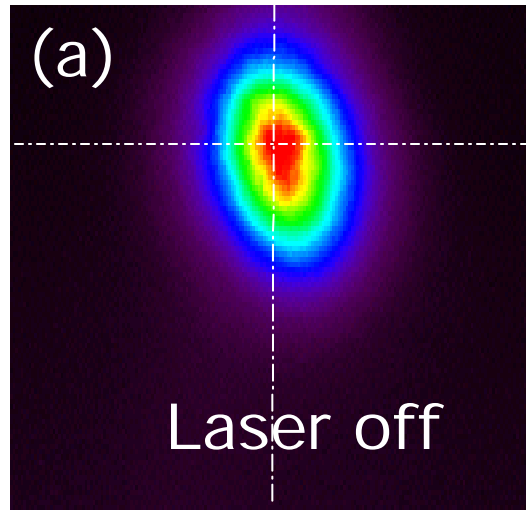


Figure 1. Muggli, et al.

Experiment



PIC Simulation

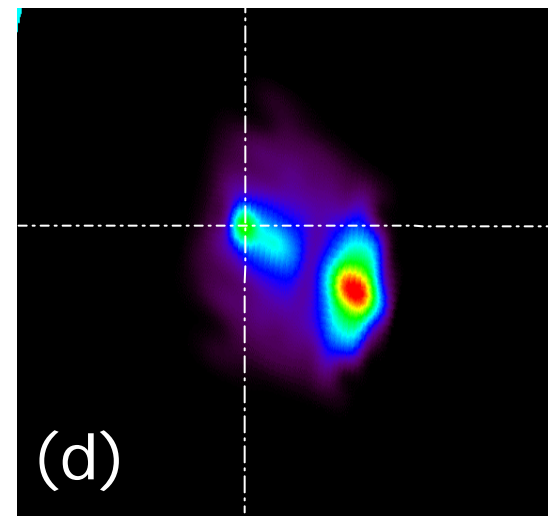
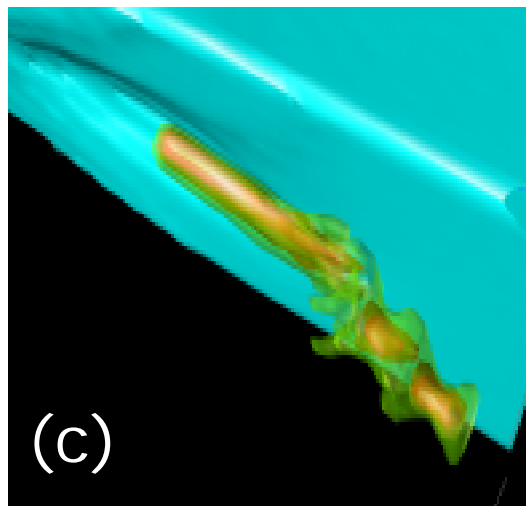


Figure 2. Muggli, et al.

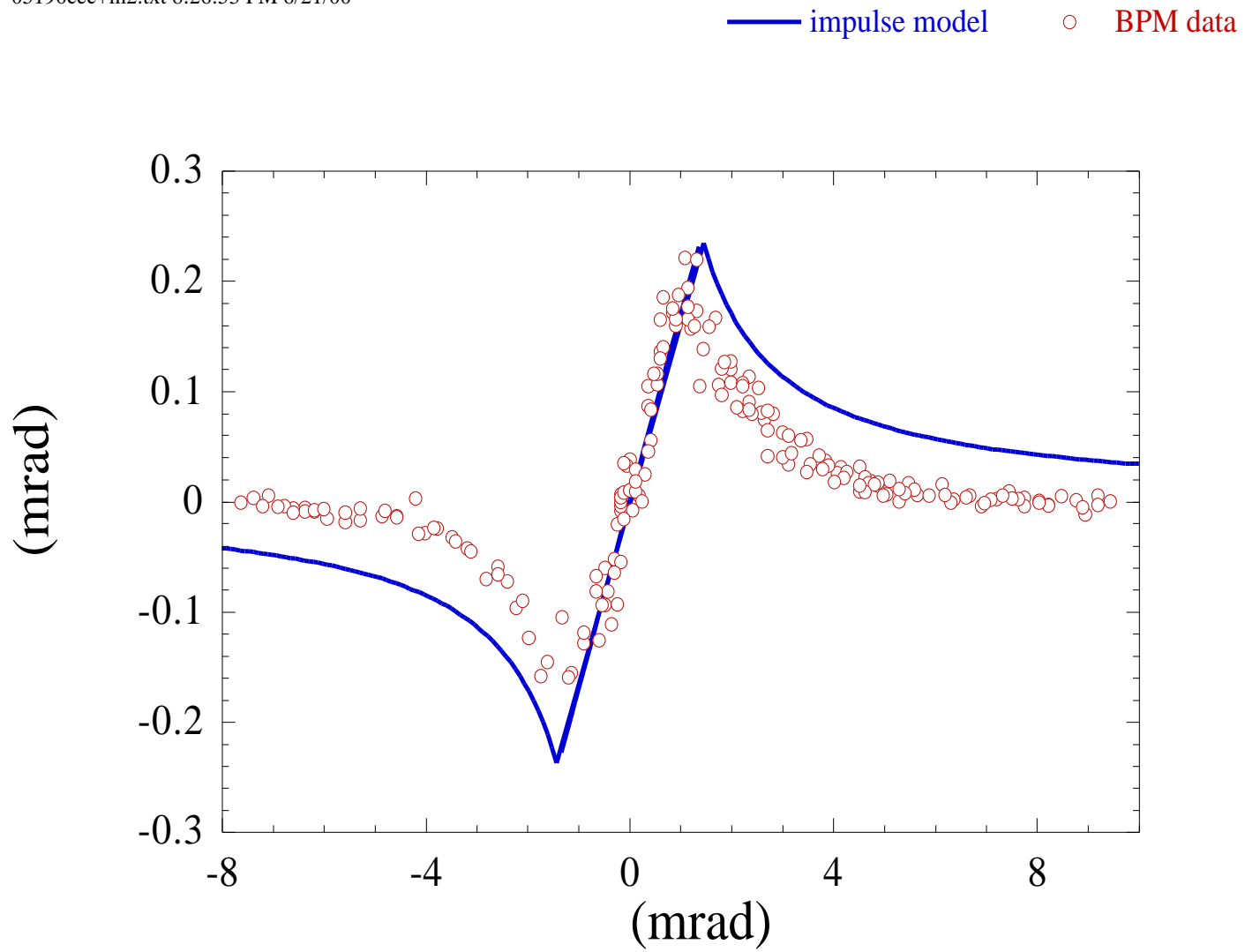


Figure 3. Muggli, et al.